



**PRODUCTION OF MOSIB ALLOYS BY
SPARK PLASMA SINTERING METHOD**

Master's Thesis

Buse KATIPOĞLU

Eskişehir 2024

**PRODUCTION OF MOSIB ALLOYS BY SPARK PLASMA SINTERING
METHOD**

Buse KATIPOĞLU

Master's Thesis

Department of Materials Science and Engineering

Supervisor: Assoc.Prof.Dr Erhan AYAS

Eskişehir

Eskişehir Technical University

Institute of Graduate Programs

August 2024

FINAL APPROVAL FOR THESIS

This thesis titled PRODUCTION OF MOSIB ALLOYS BY SPARK PLASMA SINTERING METHOD has been prepared and submitted by Buse KATIPOĞLU in partial fulfillment of the requirements in "Eskişehir Technical University Directive on Graduate Education and Examination" for the Degree of Master's in Materials Science and Engineering Department has been examined and approved on 14/08/2024.

<u>Committee Members</u>	<u>Title, Name and Surname</u>	<u>Signature</u>
Member	: Assoc. Prof. Dr Erhan AYAS	
Member	: Prof. Dr. Güray KAYA	
Member	: Assoc. Prof. Dr Ali ÇELİK	

Prof. Dr. Semra KURAMA
Director of the Institute of Graduate Programs

14/08/2024

SUPERVISOR APPROVAL

Master's student Buse KATIPOĞLU, whom I supervise, has completed this thesis titled PRODUCTION OF MOSIB ALLOYS BY SPARK PLASMA SINTERING METHOD. According to my inspections, the work is scientifically and ethically appropriate for the student to the thesis defense exam.

Supervisor

Assoc.Prof.Dr Erhan AYAS



ABSTRACT

PRODUCTION OF MOSIB ALLOYS BY SPARK PLASMA SINTERING METHOD

Buse KATIPOĞLU

Department of Materials Science and Engineering

Eskişehir Technical University, Institute of Graduate Programs, August 2024

Supervisor: Assoc.Prof.Dr Erhan AYAS

This study investigates the fabrication of MoSiB alloys, which consist of a three-phase mixture: molybdenum solid solution (Mo_{ss}) and the intermetallic phases Mo_3Si (A15), Mo_5SiB_2 (T2), and Mo_5Si_3 (T1). The goal is to produce both undoped and SiC whisker-doped compositions using spark plasma sintering (SPS). This process examines the formation of intermetallics and the distribution of whisker-based additives within the microstructure. Powdered samples were mixed using a ball mill and an ultrasonic bath, then sintered at 1600°C under a coaxial pressure of 40 MPa for 30 minutes. This temperature corresponds to the isothermal temperature in the MoSiB phase diagram. Although intermetallic phases formed, the samples did not achieve the theoretical density. The Vickers hardness values ranged from 13.84 to 18.10 GPa, and the fracture toughness values ranged from 1 to $3 \text{ MPa}\cdot\text{m}^{1/2}$. The inclusion of SiC whiskers increased the hardness but also resulted in higher porosity. Oxidation and microstructural stability tests were conducted at 1300°C in air, with four cycles of 6 hours each followed by approximately 2 hours of cooling. The results showed that the stability of these samples was comparable to the best values reported in existing literature.

Keywords: MoSiB, Spark Plasma Sintering, Characterization, SiC whisker, Alloys.

ÖZET

SPARK PLAZMA SİNTERLEME METODU İLE MOSİB ALAŞIMLARININ ÜRETİMİ

Buse KATIPOĞLU

Malzeme Bilimi ve Mühendisliği Anabilim Dalı

Eskişehir Teknik Üniversitesi, Lisansüstü Eğitim Enstitüsü, Ağustos 2024

Danışman: Doç. Dr. Erhan AYAS

Bu çalışma, molibden katı çözültisi (Mo_{ss}) ve Mo_3Si (A15), Mo_5SiB_2 (T2) ve Mo_5Si_3 (T1) intermetalik fazlarını içeren üç fazlı bir karışımdan oluşan MoSiB alaşımlarının üretimini araştırmaktadır. Amacımız, hem katkısız hem de SiC whisker katkılı kompozisyonları kıvılcım plazma sinterleme (SPS) kullanarak üretmektir. Bu süreç, intermetaliklerin oluşumunu ve whisker bazlı katkı maddelerinin mikroyapı içerisindeki dağılımını incelemektedir. Toz numuneler, bir bilyalı öğütücü ve ultrasonik banyo kullanılarak karıştırılmış, ardından $1600^{\circ}C$ 'de, 30 dakika süreyle 40 MPa'lık eksenel basınç altında sinterlenmiştir. Bu sıcaklık, MoSiB faz diyagramındaki izotermal sıcaklığa karşılık gelmektedir. İntermetalik fazlar oluşmasına rağmen, numuneler teorik yoğunluğa ulaşamamıştır. Vickers sertlik değerleri 13.84 ile 18.10 GPa arasında, kırılma tokluğu değerleri ise 1 ile 3 $MPa \cdot m^{1/2}$ arasında değişmiştir. SiC whiskerlerin eklenmesi sertliği artırmış, ancak daha yüksek poroziteye de yol açmıştır. Oksidasyon ve mikroyapısal stabilite testleri, havada $1300^{\circ}C$ 'de, her biri yaklaşık 2 saatlik soğuma süresiyle dört döngü boyunca 6 saat sürdürülmüştür. Sonuçlar, bu numunelerin stabilitesinin mevcut literatürde bildirilen en iyi değerlere kıyasla benzer olduğunu göstermiştir.

Anahtar Sözcükler: MoSiB, Spark Plazma Sinterleme, Karakterizasyon, SiC visker, Alaşım.

ACKNOWLEDGEMENTS

I would like to express my deepest gratitude to my advisor, Assoc. Prof. Dr. Erhan AYAS, for his invaluable advice, support, and significant contribution to my study and professional growth.

I am grateful to my friend TEI Engineer Eda METİN for her contributions to my experimental studies during my thesis research.

I would like to thank TEI technicians Göksel ÖREN, Mahmut Naci UĞUR, Nusret Emre GÜNDÜZ and İlkey BİRGÜL for their assistance about cutting, grinding and oxidation testing of samples.

I would like to thank TEI Materials and Processes Development Laboratory staff for assisting in metallurgical and mechanical tests.

I am deeply appreciative of TEI Senior Technical Leader Rifat Yılmaz for generously sharing their experience in patterning.

I would like to extend my endless thanks to my esteemed parents, who have taught me to adopt respect and love as a principle since my childhood, and who have never withheld their support from me.

Buse KATİPOĞLU

STATEMENT OF COMPLIANCE WITH ETHICAL PRINCIPLES AND RULES

I hereby truthfully declare that this thesis is an original work prepared by me; that I have behaved in accordance with the scientific ethical principles and rules throughout the stages of preparation, data collection, analysis and presentation of my work; that I have cited the sources of all the data and information that could be obtained within the scope of this study, and included these sources in the references section; and that this study has been scanned for plagiarism with “scientific plagiarism detection program” used by Eskişehir Technical University, and that “it does not have any plagiarism” whatsoever. I also declare that, if a case contrary to my declaration is detected in my work at any time, I hereby express my consent to all the ethical and legal consequences that are involved.

Buse KATİPOĞLU

CONTENTS

	<u>Page</u>
HEADER PAGE	I
FINAL APPROVAL FOR THESIS	II
SUPERVISOR APPROVAL	III
ABSTRACT.....	IV
ÖZET	V
ACKNOWLEDGEMENTS	VI
STATEMENT OF COMPLIANCE WITH ETHICAL PRINCIPLES AND RULES	VII
CONTENTS	VIII
LIST OF TABLES	X
LIST OF FIGURES	XI
GLOSSARY OF SYMBOLS AND ABBREVIATIONS	XV
1. INTRODUCTION	1
1.1. Molybdenum Silicides.....	1
1.2. MoSiB Ternary Alloys	2
2. MECHANICAL PROPERTIES OF MOSIB ALLOYS	7
2.1. Strength and Mechanical Properties of MoSiB Alloys	7
2.2. Oxidation Mechanism Of MoSiB Alloys	9
3. APPLICATIONS OF MO AND MOSIB TERNARY ALLOYS.....	12
3.1. Lighting	13
3.2. X-Ray Tubes	14
3.3. Hot Working.....	15
4. PROCESSING ROUTES OF MOSIB ALLOYS.....	16
4.1. Arc Melting.....	16
4.2. Hot Working.....	17

4.3. Powder Metallurgy.....	18
5. EXPERIMENTAL WORK.....	21
5.1. Selection Of Composition	21
5.2. Preparation Of Powder Mixture	22
5.3. Spark Plasma Sintering Procedure	27
6. EXPERIMENTAL RESULTS.....	31
6.1. Density Measurement	31
6.2. Phase And Microstructure Analysis.....	33
6.3. Hardness And Fracture Toughness Measurement	42
6.4. Oxidation Test	47
6.5. Thermal Analysis	52
7. CONCLUSION AND FUTURE WORK	57
REFERENCES.....	59
CURRICULUM VITAE	

LIST OF TABLES

	<u>Page</u>
Table 1.1. Physical and mechanical properties of the Mo _{ss} phase and the intermetallic phases Mo ₃ Si and Mo ₅ SiB ₂ (D. Sturm, 2007), (Mitra, 2006), (J.H. Schneibel C. L., 1999), (J.H. Schneibel J. K., 2003)	6
Table 5.1. Experimental powder properties	22
Table 5.2. (Continued) Process parameters of SPS	28
Table 5.3. (Continued) Process parameters of SPS	29
Table 6.1. Density values for all samples	32
Table 6.2. Hardness and fracture toughness value of all samples.....	44

LIST OF FIGURES

	<u>Page</u>
<p>Figure 1.1. The Moss-A15-T2 phase field is highlighted in the isothermal area of the Mo-rich part of the MoSiB phase diagram at 1600°C. A triangle designates the T2 phase's stoichiometric composition. (J.H. Perepezko, Phase Stability in Processing and Microstructure Control in High Temperature Mo-Si-B Alloys, 2001).....</p>	3
<p>Figure 1.2. The crystal forms of molybdenum (a), A15 (b), and T2 (c) (J.H. Perepezko, Phase Stability in Processing and Microstructure Control in High Temperature Mo-Si-B Alloys, 2001).....</p>	4
<p>Figure 1.3. Isothermal section of the ternary MoSiB system at 1600 °C [(H. Nowotny, 1957), (R. Sakidja J. P., 2008) The Mo-rich compositions that highlight both of the significant triangles that Berczik et al. (Patent No. 5,595,616, 1997) (Patent No. 5,693,156, 1997) and Akinc et al. (M. Akinc, 1999), (Akinc, 1996)</p>	5
<p>Figure 1.4. Development of turbine materials designed for increased operating temperatures, with the application limit of Ni-based superalloys delineated by a straight line (J.E. Jackson, 2007)</p>	6
<p>Figure 2.1. The temperature dependency of the ultimate tensile strength (○), 0.2% yield strength (□), and elongation-to-fracture (Δ) of the Mo₃Si₁B weight percent alloy is illustrated in Figure 2.16. Jéhanno et al. synthesized the material using hot-isostatic pressing of powder generated by inert gas atomization. (P. Jéhanno M. H., 2004)</p>	7
<p>Figure 2.2. The ultimate tensile strength of Mo-3Si-1B wt.% alloys in both the as-HIPed and extruded states is compared to data from a commercial molybdenum alloy and a single crystal Ni-based superalloy, as reported by Jéhanno et al. (P. Jéhanno M. H., 2005).....</p>	8
<p>Figure 2.3. The room temperature fracture toughness of molybdenum as a function of silicon concentration, as observed by Sturm et al. The equilibrium concentration of silicon at 1600°C is 0.87 wt.%. (D. Sturm, 2007)</p>	9

Figure 2.4. Schematic representation of the oxidation processes proposed by Akinc and Meyer for (a) a porous, low viscosity scale and (b) a low porosity, high viscosity scale. (Dimiduk, 2003)	10
Figure 2.5. The various kinetic oxidation regimes for molybdenum and MoSiB alloys, as proposed by Parthasarathy et al.. (T.A. Parthasarathy, 2002).....	11
Figure 3.1. Schematic representation of the lamp.....	14
Figure 3.2. X-ray target displaying rotor (A), stem (B), and molybdenum-alloy target (C) with tungsten-rhenium alloy track (D) for X-ray production. The graphite heat sink (E) and the cathode cup (F), which houses the tungsten filament © Plansee SE (X-ray tube manufactured by Dunlee), are also depicted.....	15
Figure 4.1. The MoSiB phase diagram showing the liquidus projection for the Mo-rich area, with the various zones of primary solidification highlighted (Nunes et al., 2018). In point I1, we can see the Moss-A15-T2 invariant eutectic. (C.A. Nunes, 2000).....	17
Figure 4.2. Two arc-melted alloys, Mo-13Si-15B and Mo-9.6Si-14.2B, were imaged using BSE in their as-cast form (C.A. Nunes, 2000). Note the images are shown at different magnifications	17
Figure 4.3. Pratt & Whitney (East Hartford, CT) developed a Moss-T2 alloy that had a continuous molybdenum matrix. Extrusion was used to solidify a super-saturated Moss powder that had been rapidly solidified. Separate dispersoids of T2 were precipitated from a Moss matrix by means of a controlled heat treatment. (P. Jéhanno M. H., 2004).....	18
Figure 4.4. A BSE micrograph depicting a Mo-9.4Si-13.8B at.% alloy, meticulously prepared by Nieh et al. through the hot pressing of elemental powders of molybdenum, silicon, and boron. The dark areas present in the image represent silica inclusions. (T.G. Nieh, 2001)	19
Figure 5.1. Schematic figure of experimental procedure.....	21
Figure 5.2. SEM images of Mo powder.....	22
Figure 5.3. SEM images of crystalline B powder	23
Figure 5.4. SEM images of crystalline SiC whisker	23
Figure 5.5. Planetary ball mill (a) and (b) schematic of cataract movement during milling	24

Figure 5.6. a) BSE images of 3000x magnification and b) BSE images of 10000x magnification M10Si matrix powder	24
Figure 5.7. BSE images of M5SiC20 powder mixture	25
Figure 5.8. BSE images of M3.3SiC15 powder mixture	25
Figure 5.9. BSE images of M10SiC2 powder mixture	26
Figure 5.10. BSE images of M10SiC5 powder mixture	26
Figure 5.11. BSE images of M10SiC8 powder mixture	27
Figure 5.12. Setup for spark plasma sintering technology (SPS) at the Eskişehir Technical University (ESTÜ) Eskişehir, Turkey (a) structure of the SPS (b) schematic structure according to (c) SPS tooling design	29
Figure 6.1. XRD pattern of the pure Mo.....	34
Figure 6.2. XRD pattern of the pure Si.....	34
Figure 6.3. XRD pattern of the pure B.....	35
Figure 6.4. XRD pattern of the M10Si	35
Figure 6.5. BSE images of M10Si SPSed sample	36
Figure 6.6. SEM-EDS spectrum analysis of M10Si SPSed sample	37
Figure 6.7. SEM-EDS spectrum analysis of M10Si SPSed sample	38
Figure 6.8. SEM images of M5SiC20 SPSed sample.....	38
Figure 6.9. SEM images of containing non-homogenous SiC whisker M5SiC20 SPSed sample.....	38
Figure 6.10. BSE images of M10SiC2 SPSed sample.....	39
Figure 6.11. (Continued) SEM-EDS spectrum analysis of M10SiC2 SPSed sample	39
Figure 6.12. (Continued) SEM-EDS spectrum analysis of M10SiC2 SPSed sample	40
Figure 6.13. (Continued) SEM-EDS mapping analysis of M10SiC2 SPSed sample	40
Figure 6.14. (Continued) SEM-EDS mapping analysis of M10SiC2 SPSed sample	41
Figure 6.15. BSE images of M10SiC5 SPSed sample.....	41
Figure 6.16. (Continued) SEM-EDS spectrum analysis of M10SiC5 SPSed sample	41

Figure 6.17. (Continued) SEM-EDS spectrum analysis of M10SiC5 SPSed sample	42
Figure 6.18. BSE images of M10SiC8 SPSed sample.....	42
Figure 6.19. Schematic representation of the Vickers indent on the sample surface	43
Figure 6.20. Example of Vickers indentation image of M5SiC20	44
Figure 6.21. Example of Vickers indentation image of M10SiC2	45
Figure 6.22. Example of Vickers indentation image of M10SiC5	45
Figure 6.23. Example of Vickers indentation image of M10SiC8	46
Figure 6.24. Mass loss curve of M10Si at 1300°C	48
Figure 6.25. Mass loss curves of M10SiC2, M10SiC5 and M10SiC8 at 1300°C	48
Figure 6.26. Specimen oxidized surface modification of M10SiC2.....	49
Figure 6.27. Specimen oxidized surface modification of M10SiC5.....	50
Figure 6.28. Specimen oxidized surface modification of M10SiC8.....	50
Figure 6.29. Oxidation of the Mo3Si1B wt.% alloy compared to similar test reported in the literature (R. Sakidja F. R., 2006). The error bars for the Georgia Tech data are within the data points.....	51
Figure 6.30. Combined TGA/DTA traces of all samples heated at 10 K/min in an atmosphere of N₂/O₂	54
Figure 6.31. Combined TGA/DTA traces of M10SiC2 heated at 10 K/min in an atmosphere of N₂/O₂	54
Figure 6.32. Combined TGA/DTA traces of M10SiC5 heated at 10 K/min in an atmosphere of N₂/O₂	55
Figure 6.33. Combined TGA/DTA traces of M10SiC8 heated at 10 K/min in an atmosphere of N₂/O₂	55
Figure 6.34. Combined TGA/DTA traces of M10Si heated at 10 K/min in an atmosphere of N₂/O₂	56

GLOSSARY OF SYMBOLS AND ABBREVIATIONS

B	: Boron
bcc	: Body centered cubic
BSE	: Backscattered scanning electron
°C	: Celcius degree
CIP	: Cold isostatic pressing
CT	: Computerized axial tomography
DBTT	: Ductile to brittle transition temperature
DTA	: Differential thermal analysis
DSC	: Differential scanning calorimetry
EDS	: Energy dispersive spectroscopy
FAST	: Field assisted sintering
g	: gram
Gpa	: Gigapascal
HIP	: Hot isostatic pressing
Hv	: Hardness of Vickers
K	: Kelvin degree
KIc	: Fracture toughness
mm	: millimeter
Mo	: Molybdenum
Mo _{ss}	: Molybdenum solid solution
Mo ₃ Si	: A15 phase
Mo ₅ Si ₃	: T1 phase
Mo ₅ SiB ₂	: T2 phase
MoO ₃	: Molybdenum oxide
MHC	: Molybdenum hafnium carbon alloy
Mpa	: Megapascal
Pa	: Pascal
rpm	: Rotate per minute
SEM	: Scanning electron microscopy
SPS	: Spark plasma sintering
Si	: Silicon

SiC	:	Silicon carbide
TGA	:	Thermal gravimetric analysis
TZM	:	Titanium zirconium molybdenum alloy
%at	:	Atomic percent
%wt	:	Weight percent
%vol	:	Volume percent
μ	:	Micrometer



1. INTRODUCTION

Although they have higher melting points and better mechanical properties at high temperatures, refractory metals—like molybdenum—are constrained by their insufficient resistance to oxidation. MoSiB ternary alloys have attracted lots of attention and offer a potential solution. Because a protective silicate layer forms, molybdenum-based silicides are particularly known for their resistance to oxidation. Nowotny first drew the MoSiB phase diagram in 1957, and Perepezko later updated it in 2001. (J.H. Perepezko, *Phase Stability in Processing and Microstructure Control in High Temperature Mo-Si-B Alloys*, 2001). Berczik's pioneering research concentrated on MoSiB-based compositions, namely inside the molybdenum-rich area of the phase diagram, with the objective of developing gas turbine blades. (Patent No. 5,595,616, 1997), (Patent No. 5,693,156, 1997). The molybdenum solid solution (Moss) and the two intermetallic phases Mo₃Si (A15) and Mo₅SiB₂ (T2) make up the three-phase region where the alloys of interest are found. All three phases are excellent choices especially for high-temperature applications because they have melting points higher than 2000°C and remain stable at room temperature. While the intermetallic phases increase high-temperature creep resistance and make it easier to form a protective borosilicate layer, which increases oxidation resistance, the ductile Moss phase improves fracture toughness by bridging to intergranular cracks.

The fundamental characteristics of molybdenum make it highly attractive specific for ultra-high temperature applications. It has the sixth highest melting point among all elements. Molybdenum exhibits a low thermal expansion coefficient and high thermal conductivity, providing remarkable resistance to thermal shock and fatigue. Its lower density, in comparison to tantalum and tungsten, is particularly advantageous for aerospace applications. Furthermore, niobium-based alloys are being examined as potential next-generation materials for turbine blades of gas turbine engines. (Patent No. 5,693,156, 1997), (C.A. Nunes, 2000).

1.1. Molybdenum Silicides

The intermetallics which are molybdenum and silicon are notable for their exceptional oxidation resistance. Molybdenum and silicon intermetallic compounds have three intermetallic phases: Mo₃Si, Mo₅Si₃, and MoSi₂. MoSi₂ is widely employed for its ability to withstand extended exposure to air at temperatures up to 1700°C, making it appropriate for high temperature elements. The oxidation resistance of MoSi₂ arises from

the formation of a protective SiO₂ surface layer. When heated the MoSi₂, molybdenum and silicon oxidize, leading to the evaporation of MoO₃ oxide compound and the creation of a continuous passivating layer of SiO₂. (M.K. Meyer, 1999).

Alternative intermetallic phases in the Mo-Si binary system have been examined due to the suboptimal mechanical properties of MoSi₂. The Mo₃Si phase has been investigated as a structural material; nevertheless, its oxidation resistance requires enhancement, constraining its practical employment in high-temperature environments. (D.M. Shah, 1992), (Ochiai, 2006). Mo₅Si₃ demonstrates creep rates approximately an order of magnitude lower than MoSi₂, attributable to its more intricate crystal structure. Nonetheless, it exhibits inferior oxidation resistance compared to MoSi₂. Akinc and Meyer discovered that using minor quantities of boron (1-3 wt%) can markedly improve the oxidation resistance of Mo₅Si₃, approaching the levels seen in MoSi₂. (M. Akinc, 1999). In this experiment, the incorporation of 1.24 wt.% boron diminished the oxide scale thickness from several hundred microns to below 10 μm. The use of boron significantly reduced the viscosity of the silica scale, enhancing oxidation resistance through improved surface coverage.

Pratt & Whitney's gas burner experiments have shown that molybdenum-based composites possess significant thermal shock resilience in conditions that replicate jet fuel burning. (R.E.Honnell, 1990). These materials survived even lots of cycles from room temperature to higher than 1000°C with no failures.

1.2. MoSiB Ternary Alloys

The MoSiB phase diagram was firstly developed by Nowotny and subsequently refined by Perepezko, Figure 1.1 (J.H. Perepezko, Phase Stability in Processing and Microstructure Control in High Temperature Mo-Si-B Alloys, 2001). In addition to the binary intermetallic phase, a ternary intermetallic phase designated as Mo₅SiB₂ is present. Preliminary experiments into high-temperature structural applications focused on the Mo₃Si (A15), Mo₅Si₃ (T1), and Mo₅SiB₂ (T2) phase domains. The intermetallics in this system exhibit superior mechanical properties and creep resistance compared to MoSi₂; however, they are insufficient under high-stress circumstances due to reduced fracture toughness. Recent efforts have shifted attention to the Mo₅SiB₂-A15-T2 intermetallic phase triangle. The mechanical characteristics of these alloys have been enhanced by including a more ductile molybdenum solid solution phase. Berczik pioneered the study of MoSiB alloys for jet engine applications, filing a patent in 1997

for alloys with compositions containing at least 1.0-4.5% silicon and at least 0.5-4.0% boron by weight. (Patent No. 5,595,616, 1997), (Patent No. 5,693,156, 1997). The alloys of interest in this study are situated within the highlighted region of the phase diagram, Figure 1.1. The isothermal phase diagram is established at 1600°C; yet, this three-phase area remains stable down to ambient temperature, exhibiting only minor fluctuations in the solid solution boundaries of the phases.

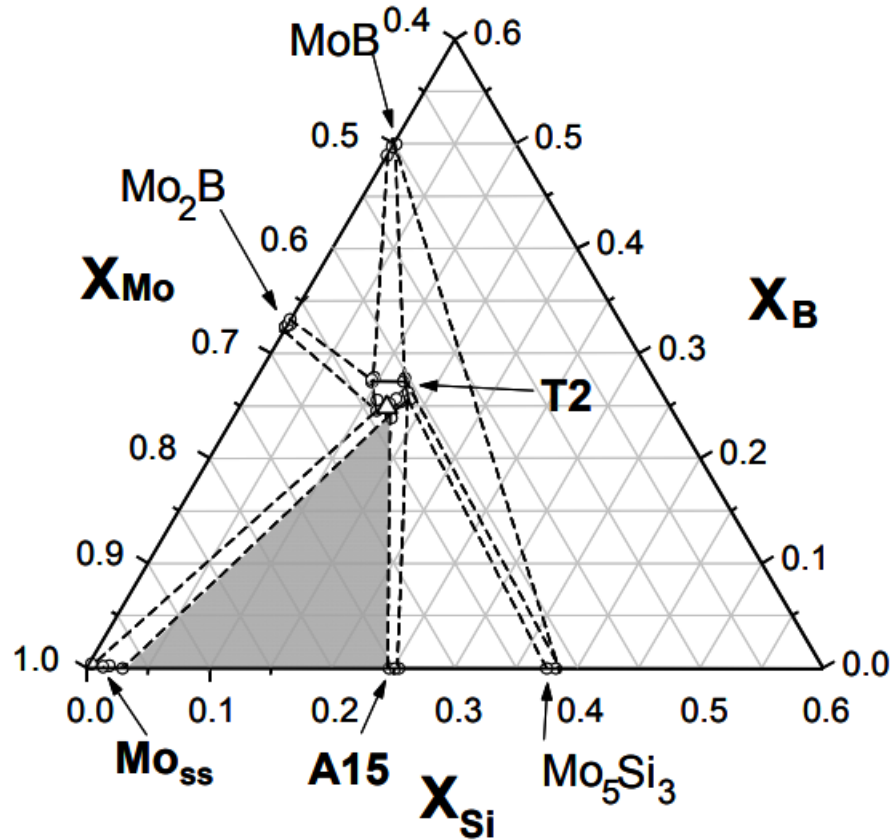


Figure 1.1. The Moss-A15-T2 phase field is highlighted in the isothermal area of the Mo-rich part of the MoSiB phase diagram at 1600°C. A triangle designates the T2 phase's stoichiometric composition. (J.H. Perepezko, *Phase Stability in Processing and Microstructure Control in High Temperature Mo-Si-B Alloys*, 2001)

As depicted in Figure 1.2. Molybdenum exhibits a body-centered cubic (BCC) crystal structure, as seen by its atomic arrangement. The molybdenum-silicon binary phase diagram reveals that silicon has limited solubility in molybdenum, reaching a maximum of around 4 atomic percent (at.%) at a peritectic temperature of 2025°C. The molybdenum-boron binary phase diagram indicates that boron exhibits negligible solubility in molybdenum at temperatures under 1600°C. At the eutectic temperature of 2175°C, the solubility limit of boron in molybdenum is around very low. The molybdenum-silicon binary phase diagram indicates that silicon has limited solubility in

molybdenum, reaching a maximum of around 4 atomic percent (at.%) at a peritectic temperature of 2025°C. The molybdenum-boron phase diagram demonstrates that boron's solubility in molybdenum is negligible at processing temperatures below 1600°C. At the eutectic temperature of 2175°C, the solubility of boron in molybdenum is constrained to approximately low percentage. (Liao, 1988). The Mo₃Si phase, referred to as A15 due to its crystal structure, possesses a body-centered cubic (BCC) unit cell with six molybdenum atoms and two silicon atoms. Preliminary phase diagrams suggested that Mo₃Si is a stoichiometric line compound; nevertheless, investigations by Rosales and Schneibel demonstrated that its composition displays slight variations. In equilibrium with molybdenum, Mo₃Si contains around 20 atomic percent (at.%) silicon. (Schneibel, 2000)

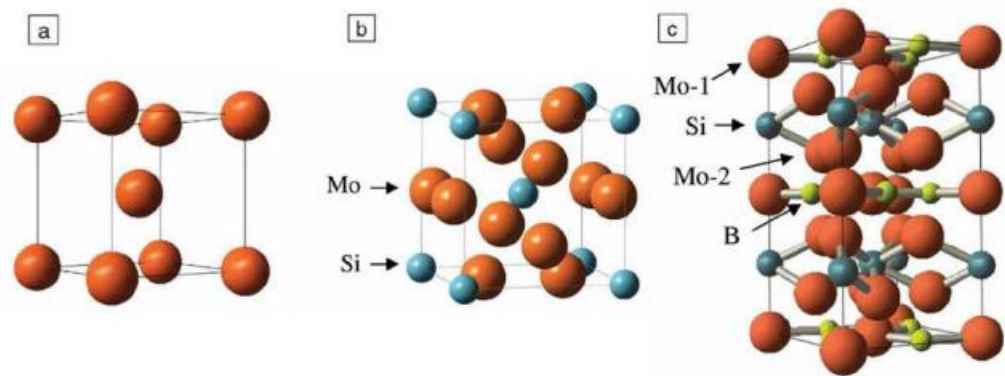


Figure 1.2. The crystal forms of molybdenum (a), A15 (b), and T2 (c) (J.H. Perepezko, *Phase Stability in Processing and Microstructure Control in High Temperature Mo-Si-B Alloys*, 2001)

Another highlighted region in Figure 1.3 is referred to as the "Berczik triangle," named after the investigations conducted by Berczik et al. (Patent No. 5,693,156, 1997). As illustrated in the Figure 1.3, the Berczik triangle is situated between the Mo_{ss} and intermetallic phases Mo₃Si and Mo₅SiB₂. As previously discussed, the Mo-Si and MoSiB intermetallic phases within the MoSiB system improve the alloy's creep resistance and oxidation behavior at high operating temperatures. (Ritchie, *Mo-si-b alloys for ultrahigh-temperature structural applications*, 2012), (T.A. Parthasarathy, 2002), (J.H. Schneibel M. K., 2001). Nonetheless, these intermetallic-based materials present considerable obstacles for utilization in high-temperature sectors owing to their elevated brittle to ductile transition temperature (BDTT) and reduced fracture toughness at ambient temperature. (Ritchie, *Mo-si-b alloys for ultrahigh-temperature structural applications*,

2012), (Koizumi, 2004). Therefore, considering a modified combination of $\text{Mo}_{5\text{Si}}$, Mo_3Si , and Mo_5SiB_2 phases could be advantageous. (Ritchie, Mo-si-b alloys for ultrahigh-temperature structural applications, 2012), (T.A. Parthasarathy, 2002), (J.H. Schneibel M. K., 2001)). The three-phase microstructure exhibits a wide stability range up to high temperatures of around 1800°C temperature (S.H. Ha, 2012). Berczik MoSiB alloy compositions leverage the ductility of the Moss phase, hence enhancing fracture toughness at both ambient and elevated temperatures, in contrast to Akinc MoSiB alloys. The volume ratio of Moss in the alloy must be precisely calibrated for the intended application. Consequently, the Berczik phase triangle serves as the focal point of our study. The characteristics of the relevant stages are analyzed in the following sections.

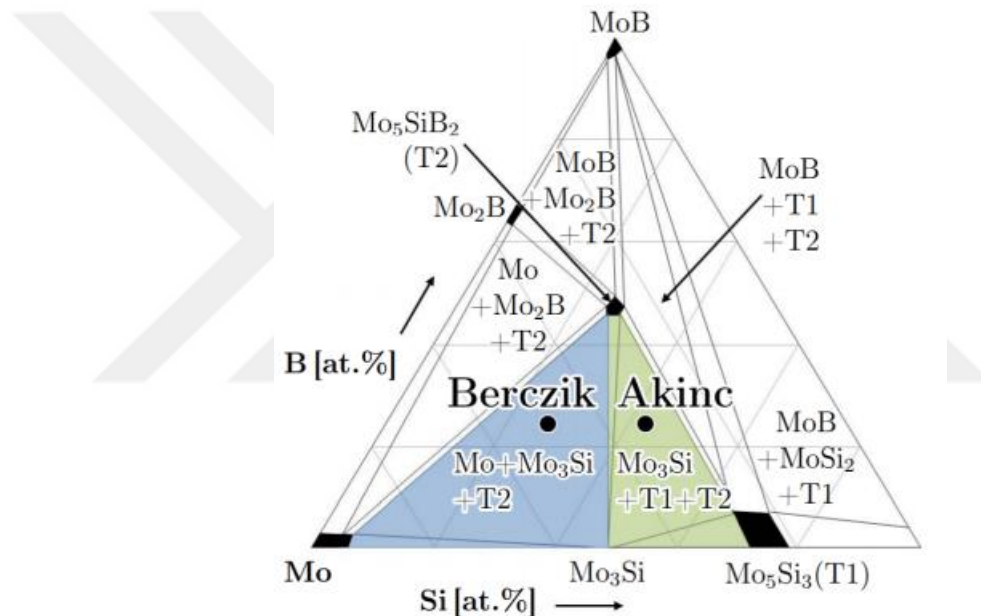


Figure 1.3. Isothermal section of the ternary MoSiB system at 1600°C [(H. Nowotny, 1957), (R. Sakidja J. P., 2008) The Mo-rich compositions that highlight both of the significant triangles that Berczik et al.. (Patent No. 5,595,616, 1997) (Patent No. 5,693,156, 1997) and Akinc et al. (M. Akinc, 1999), (Akinc, 1996)

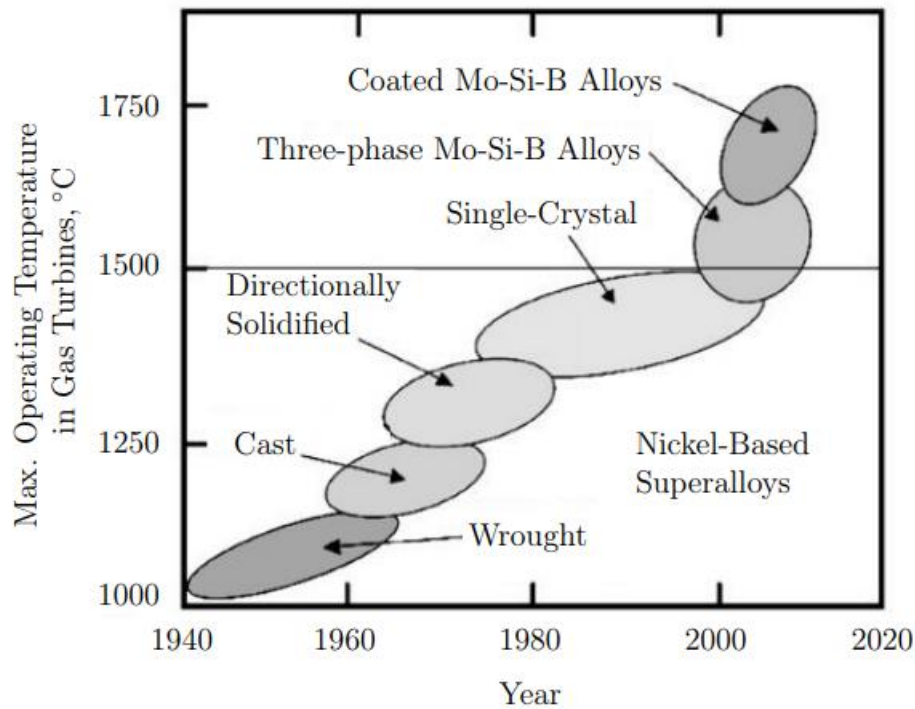


Figure 1.4. Development of turbine materials designed for increased operating temperatures, with the application limit of Ni-based superalloys delineated by a straight line (J.E. Jackson, 2007)

The structure of the three intermetallic phases offers extensive stability, even at elevated temperatures over 1600°C, hence improving creep resistance. Unlike previous approaches, such alloy compositions may exhibit reduced oxidation resistance while providing a notable advantage. The volume fraction and distribution of these microstructural components significantly enhance fracture toughness at both ambient and high temperatures. This microstructure's endurance at temperatures above 1600°C ensures improved creep resistance; despite a potential reduction in oxidation resistance, the overall mechanical toughness is markedly boosted across temperature ranges due to careful phase equilibrium. (Krüger, 2015).

Table 1.1. Physical and mechanical properties of the Mo_{55} phase and the intermetallic phases Mo_3Si and Mo_5SiB_2 (D. Sturm, 2007), (Mitra, 2006), (J.H. Schneibel C. L., 1999), (J.H. Schneibel J. K., 2003)

	Mo_{55}	Mo_3Si (A15)	Mo_5SiB_2 (T2)	Mo_5Si_3 (T1)
Crystal Structure	Bcc (A2)	Cubic (A15)	Tetragonal (D8 ₁)	Tetragonal (D8 ₁)
Melting Point, °C	2623	2025	2160–2200	2180
Density, g/cm ³	10.21	8.98	8.76	8.19
Young's Modulus, GPa	324	295	383	-
K_{Ic} , MPa√m	24	3	1.5–2	-

2. MECHANICAL PROPERTIES OF MOSIB ALLOYS

The mechanical characteristics of MoSiB alloys exhibit significant variation based on intermetallic content; hence, the reviewed study concentrates on compositions with elevated proportions of the Moss phase. The comparison of alloys generated by various processes highlights the crucial influence of microstructural morphology on mechanical characteristics.

2.1. Strength and Mechanical Properties of MoSiB Alloys

Jéhanno et al. conducted high temperature tensile testing on the alloy shown in Figure 2.2, which was produced by gas atomization process and featured a coarse dispersion of molybdenum within an intermetallic matrix (P. Jéhanno M. H., 2004). The alloy's strength and elongation and fracture values are plotted in Figure 2.1 for tests conducted at a low strain rate.

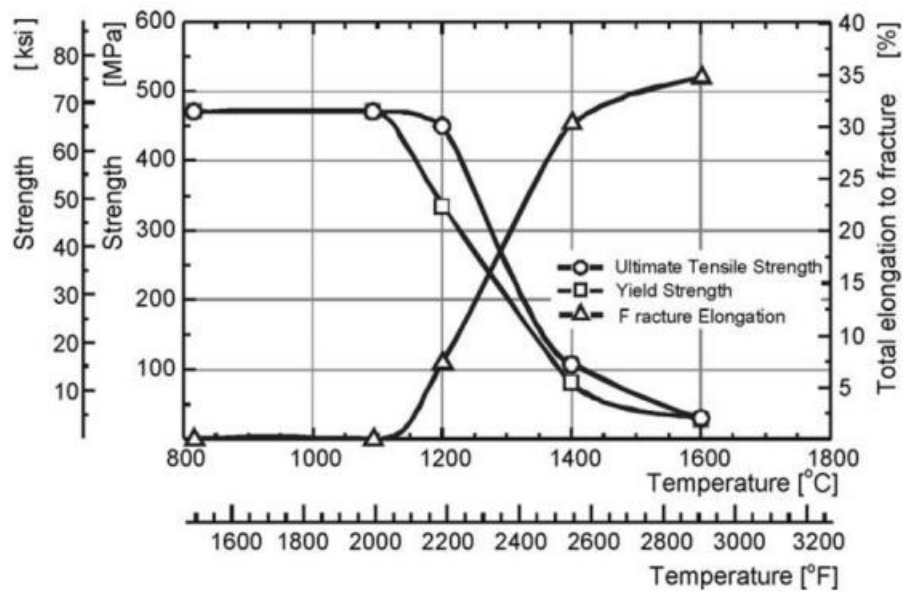


Figure 2.1. The temperature dependency of the ultimate tensile strength (\circ), 0.2% yield strength (\square), and elongation-to-fracture (Δ) of the Mo₃SiB weight percent alloy is illustrated in Figure 2.16. Jéhanno et al. synthesized the material using hot-isostatic pressing of powder generated by inert gas atomization. (P. Jéhanno M. H., 2004)

The molybdenum based alloy has a high brittle to ductile transition temperature (DBTT), because of the intermetallic matrix. Jéhanno et al. successfully disrupted the intermetallic matrix through high-temperature extrusion, as shown in Figure 2.2. The ultimate tensile strength and its elongation to fracture are plotted as a function of temperature in Figure 2.1. These results are compared to those of the unextruded alloy, a

commercial molybdenum alloy, and a single crystal superalloy commonly used in jet turbine engines (P. Jéhanno M. H., 2005).

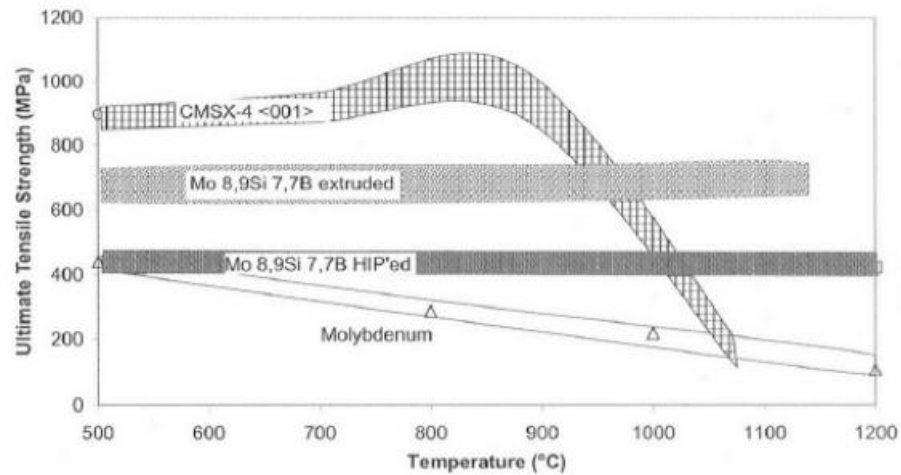


Figure 2.2. The ultimate tensile strength of Mo-3Si-1B wt.% alloys in both the as-HIPed and extruded states is compared to data from a commercial molybdenum alloy and a single crystal Ni-based superalloy, as reported by Jéhanno et al.. (P. Jéhanno M. H., 2005)

The existence of intermetallic phases significantly enhances the high-temperature strength of MoSiB alloys compared to traditional molybdenum alloys. Modifying the microstructure of MoSiB by extrusion—transitioning from an intermetallic matrix to a partially continuous Moss matrix—led to a substantial improvement in tensile strength. This alloy's low-temperature strength is inferior to that of superalloys, although it exceeds superalloys at temperatures over 1000°C. The extrusion process markedly decreased the ductile-to-brittle transition temperature (DBTT) of the MoSiB alloy by around 200°C. Nonetheless, the extruded alloy demonstrated almost no ductility at temperatures below 900°C. The lack of ductility may be attributed to the compact configuration of intermetallic particles, suggesting that further improvements in DBTT could be realized through enhanced dispersion of the intermetallic phases.

A significant drawback of molybdenum-based alloys is their vulnerability to brittleness at low temperatures. Molybdenum has little ductility due to its body-centered cubic (BCC) crystal structure, which contains slip planes for accommodating deformation. The fracture toughness of molybdenum is significantly influenced by solid solution additives. Sturm et al. investigated the effect of solid solution content on the fracture toughness of molybdenum, Figure 2.3 (D. Sturm, 2007). A notable decrease in hardness transpires with slight additions of silicon. This decrease is partially attributed to

the significant solid solution strengthening effect of silicon, which has been shown to endure at temperatures over 1200°C. (P. Jain, 2006).

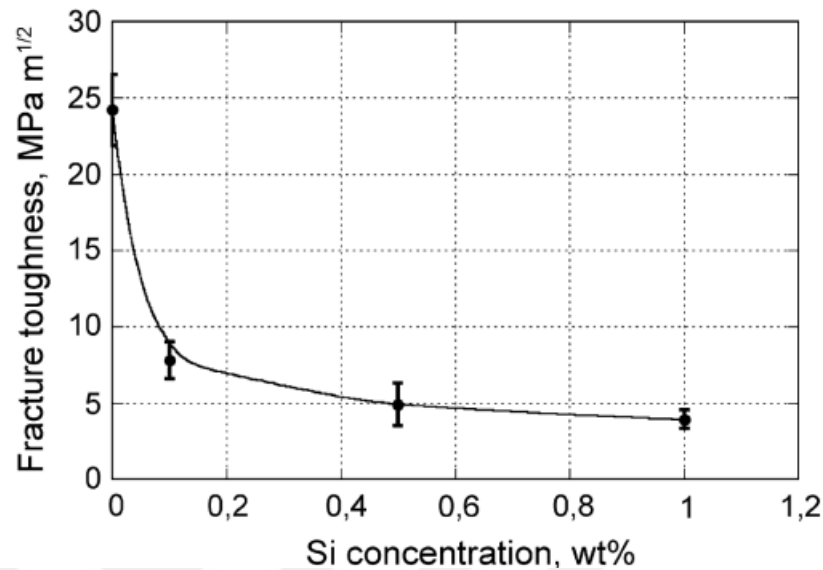


Figure 2.3. The room temperature fracture toughness of molybdenum as a function of silicon concentration, as observed by Sturm et al. The equilibrium concentration of silicon at 1600°C is 0.87 wt.%. (D. Sturm, 2007)

The reduced fracture toughness of intermetallic phases highlights the necessity to process MoSiB alloys to achieve a distribution of A15 and T2 phases within a continuous molybdenum matrix. The use of Moss particles in alloys with an intermetallic matrix improves fracture resistance through mechanisms like crack trapping and crack bridging. As the aggregation of molybdenum particles increases, the overall fracture toughness of these alloys enhances.

2.2. Oxidation Mechanism Of MoSiB Alloys

In the literature, two scenarios were proposed for the formation of the oxide scale, as illustrated in Figure 2.4. The partial pressures of oxygen at the glass-alloy contact and the pore sizes vary throughout different phases of glass scale formation. With the production of a continuous glass layer, the interface's partial pressure sufficiently decreases, facilitating the selective oxidation of silicon and boron, leading to the creation of a protective molybdenum layer. The suppression of MoO₃ formation significantly reduces mass loss due to evaporation.

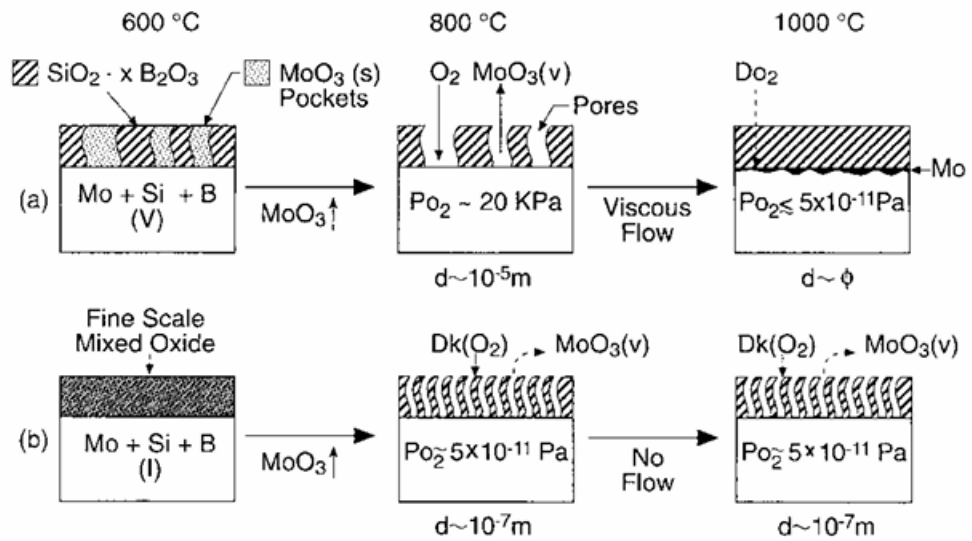


Figure 2.4. Schematic representation of the oxidation processes proposed by Akinc and Meyer for (a) a porous, low viscosity scale and (b) a low porosity, high viscosity scale. (Dimiduk, 2003)

The oxidation kinetics of MoSiB alloys are known to vary across different temperature ranges. Parthasarathy et al. studied the oxidation behavior of a Mo12Si12B wt.% alloy at various temperatures to elucidate the underlying mechanisms (T.A. Parthasarathy, 2002). The oxidation of pure molybdenum was analyzed to assess the influence of silicon and boron on oxidation resistance at low temperatures. Parthasarathy et al. indicated that the alloys exhibit either linear or parabolic oxidation rates over various temperature ranges. Linear oxidation occurred in the absence of a protective oxide layer, resulting in a mass loss rate that was directly proportional to time. The proposed oxidation kinetic behaviors are illustrated schematically in Figure 2.5. At temperatures ranging from 500°C to 600°C, pure molybdenum exhibited an increase in weight attributable to the development of a MoO_3 surface layer. MoO_3 formed a cohesive layer, leading to a parabolic increase in weight owing to its non-volatile characteristics at these temperatures. The incorporation of silicon and boron oxides in the mixed oxide scale reduced the mass gain rate for MoSiB alloys in this context.

At around 700°C, the volatilization of MoO_3 caused a linear decrease in the mass of pure molybdenum, with the rate of loss accelerating as the temperature increased. The MoSiB alloy exhibited a similar tendency of linear weight loss at equivalent temperatures; however, this characteristic was somewhat alleviated by the incorporation of silica and boron oxides. At the moderate temperature range of 650-750°C, MoSiB alloys demonstrated their lowest oxidation resistance, resulting in the formation of a porous

oxide layer that let oxygen to penetrate the interface and facilitated the evaporation of MoO_3 .

As temperatures approached 800°C , the oxidation behavior transitioned to parabolic mass loss, with the parabolic rate constant decreasing as temperature increased. The enhanced oxidation resistance observed at high temperatures is attributed to the volatilization of B_2O_3 from the borosilicate layer. This method increases the viscosity of the glass layer, hence reducing oxygen passage to the interface.

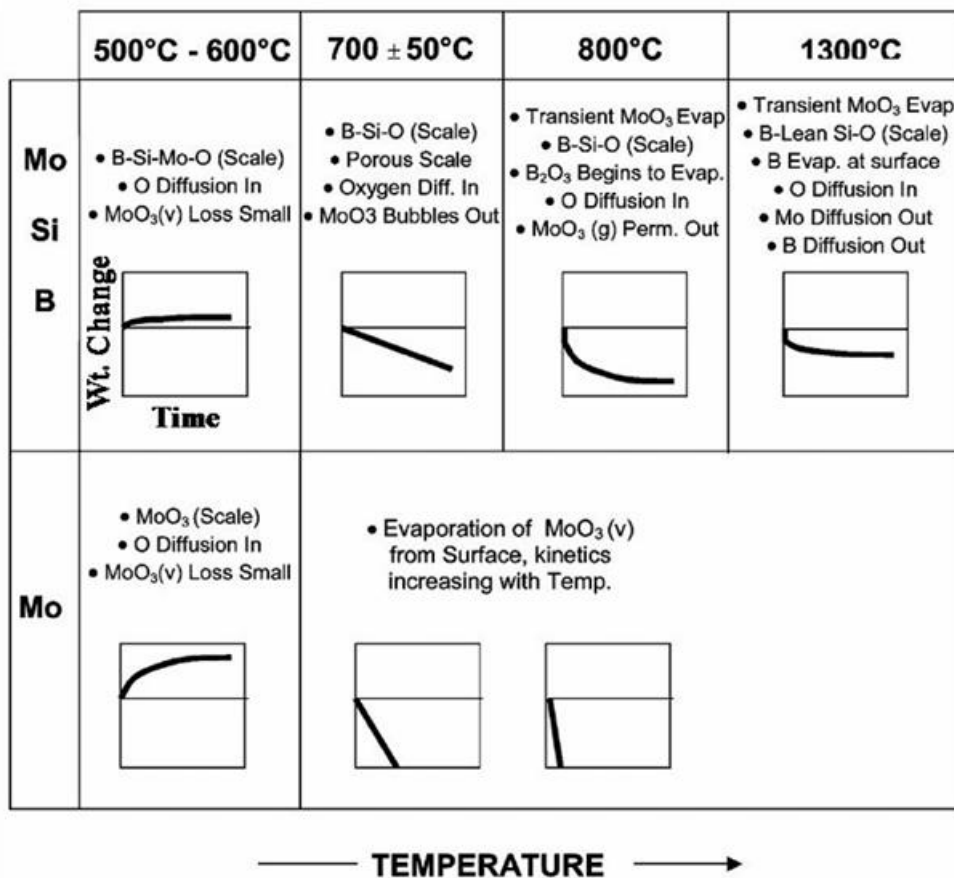


Figure 2.5. The various kinetic oxidation regimes for molybdenum and MoSiB alloys, as proposed by Parthasarathy et al.. (T.A. Parthasarathy, 2002)

3. APPLICATIONS OF MO AND MOSIB TERNARY ALLOYS

Molybdenum element is one of the particular interest for use in ultra high temperature applications due to its low coefficient of thermal expansion and high thermal conductivity, which impart good thermal shock and fatigue resistance characteristics (Baker, 1999). Molybdenum based alloys are utilized in a wide range of commercial applications, including glass melting, furnace construction, electrical interconnects, and x-ray anodes. Dispersion hardened molybdenum alloys, such as titanium, zirconium, and carbon (TZM) and hafnium and carbon (MHC) alloys, are employed under the highest temperature and stress conditions, such as in forging dies for superalloys and titanium (Schider, 1991). The mechanical and physical properties of molybdenum make it very suitable for high-temperature applications, particularly in reducing or inert atmospheres. However, molybdenum is prone to rapid oxidation under high-temperature oxidizing conditions, leading to catastrophic failure. Unlike silica and alumina, molybdenum oxide (MoO_3) does not form a protective barrier against oxidation and demonstrates instability at temperatures as low as 700°C . Efforts to enhance oxidation resistance using environmental protection coatings have had little success due to issues such as spalling or damage to the coatings. Consequently, there is considerable interest in improving the inherent oxidation resistance of molybdenum through alloying additions.

Global scientists, researchers, and engineers are engaged in intensive efforts to enhance cooling and coating technologies. These initiatives seek to reconcile the thermal resistance of nickel-based superalloys with the operational temperatures of jet engines. Professor J. H. Perepezko of the University of Wisconsin, USA, observed in a 2009 edition of the scientific journal *Science* that the cooling processes can result in considerable energy losses. Resolving this difficulty necessitates the creation of novel heat-resistant materials that exceed the performance of nickel-based superalloys, commonly known as ultra-high-temperature materials. These collaborative breakthroughs seek to enhance the inherent thermal resistance of materials to adequately satisfy the requirements of high-temperature applications. Your contributions are essential to the advancement of our scientific community.

In addition, there is a growing need for advanced technologies to process robust and refractory materials like nickel-based superalloys. While metal powder sintering is relatively straightforward, melt casting is often preferred for ultra-high temperature applications despite its challenges, such as contamination sensitivity, difficulty in

molding large parts, and strength degradation at high temperatures. However, most molybdenum alloys produced through powder sintering must overcome significant technical hurdles.

One of the pioneering efforts in exploring alternative refractory materials was the ULTMAT project, conducted in Europe from 2004 to 2008. This project focused on developing and optimizing ultra-high temperature materials to enhance performance in demanding applications, addressing the limitations of existing materials and processing techniques. Through collaborative research and innovation, the ULTMAT project aimed to advance the understanding and application of refractory materials, paving the way for future developments in high-temperature technology (Drawin, 2009). In this study, various research efforts are undertaken to improve the mechanical properties of molybdenum and niobium-based alloys by incorporating materials such as lanthanum oxide (La_2O_3), yttrium oxide (Y_2O_3), and magnesium oxide (MgO). These additions aim to enhance the alloys' performance, particularly in terms of strength, ductility, and oxidation resistance, making them more suitable for high-temperature applications.

3.1. Lighting

In the beginning, molybdenum metal was used in the lighting industry, which has a well-established history that dates back to the 1910s. As a result of its high melting point and excellent electrical conductivity, molybdenum was used by the early lighting industry in the form of wire filament supports in lamps. This was because molybdenum was designed to be an appropriate material for the filaments of incandescent light bulbs. As a component of lamps and as wire that is used as mandrels to coil tungsten filaments, lighting applications continue to account for a significant portion of the production of molybdenum metal in the present day. Halogen and high-intensity discharge (HID) lights need more sophisticated material solutions than conventional lamps do. This is because the temperatures at which they operate are substantially higher than they are for regular lamps. As a result of its high electrical conductivity and its ability to withstand high temperatures, molybdenum is an essential component of these cutting-edge lighting systems. (J.P.Wittenauer, 1993).

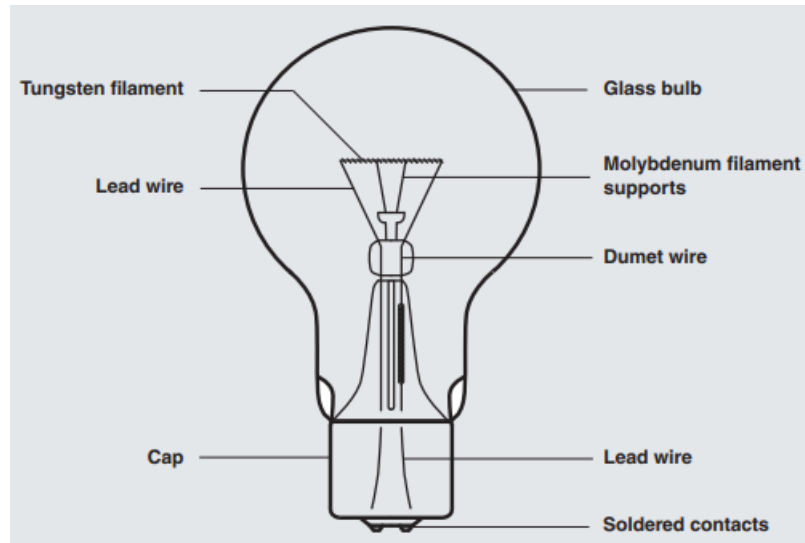


Figure 3.1. *Schematic representation of the lamp*

3.2. X-Ray Tubes

Molybdenum components are essential for the functioning of high-power X-ray tubes in computerized axial tomography (CT) scanning systems. The vacuum tube utilized for X-ray production shares similarities with those employed in early electronic devices; however, it is required to endure significantly more extreme heat and stress conditions. Figure 3.2 presents a photograph of a modern X-ray tube. The production of X-rays is facilitated by substantial electron currents and increased accelerating voltages. This process is inherently inefficient, as a substantial amount of beam energy is transformed into heat instead of X-rays. The target must endure exceptionally high temperatures. The cathode assembly employs molybdenum components, machined from mill products, to withstand the thermal loads produced by the internal filament. The rotor utilizes machined molybdenum or TZM alloy round bar, which effectively supports the spinning load of the large target and aids in heat dissipation from the target. The target is typically made from TZM or carbide-strengthened alloys similar to TZM to withstand these stresses.



Figure 3.2. X-ray target displaying rotor (A), stem (B), and molybdenum-alloy target (C) with tungsten-rhenium alloy track (D) for X-ray production. The graphite heat sink (E) and the cathode cup (F), which houses the tungsten filament © Plansee SE (X-ray tube manufactured by Dunlee), are also depicted

3.3. Hot Working

The properties of high-temperature strength and deformation resistance are essential for hot-work tooling. Molybdenum alloy tools are employed to forge superalloys within the superplastic forming temperature range, generally exceeding 1100°C. These alloys demonstrate excellent compatibility for brass extrusion, molten metal casting, and plastic injection molding applications.

Pure molybdenum exhibits compatibility with diverse molten glass compositions, making it crucial for glass handling equipment. Glass Melting Electrodes (GMEs) utilize molybdenum electrodes to conduct electric current through molten glass. This process improves energy input in fired furnaces and offers substantial productivity gains, resulting in higher throughput and efficiency. Various electrode designs exist, but they universally employ the method of submerging the molybdenum electrode in molten glass to prevent oxidation.

4. PROCESSING ROUTES OF MOSIB ALLOYS

MoSiB alloys in the three-phase field of Mo_{55}Si Mo_5SiB_2 have a higher Si/B ratio than the two phase alloys, which improves oxidation resistance rate. Several methodologies have been attempted to create these alloys with the desired combination of a continuous Mo_{55} phase and a fine intermetallic dispersion. These approaches aim to optimize the alloy's microstructure to balance mechanical properties and oxidation resistance, making them more suitable for high-temperature applications.

4.1. Arc Melting

Arc melting technology facilitates the swift and effective synthesis of various high-melting-point alloy compositions. However, it often results in a coarse microstructure and non-equilibrium states due to rapid solidification. This may lead to variations in the alloy's properties, necessitating further processing to improve the microstructure and achieve the desired equilibrium state.

Arc melting technology enables the swift and effective fabrication of various high-melting-point alloy compositions. However, it often results in a coarse microstructure and non-equilibrium conditions after rapid solidification.

MoSiB alloys, composed of molybdenum (Mo), silicon (Si), and boron (B), exhibit characteristics such as high-temperature resistance, oxidation resistance, and low density. Arc melting is an essential process utilized in the fabrication of these alloys. The method involves the fusion of materials using an electric arc within a controlled, high-temperature environment, ensuring precise amalgamation and melting of different components to obtain the desired properties.

Numerous studies have utilized the arc melting technique to investigate three-phase MoSiB alloys. Nunes et al. outlined the liquidus surface projection for the molybdenum-rich portion of the MoSiB phase, providing critical insights into the melting and solidification properties of these alloys. Figure 4.1. (C.A. Nunes, 2000).

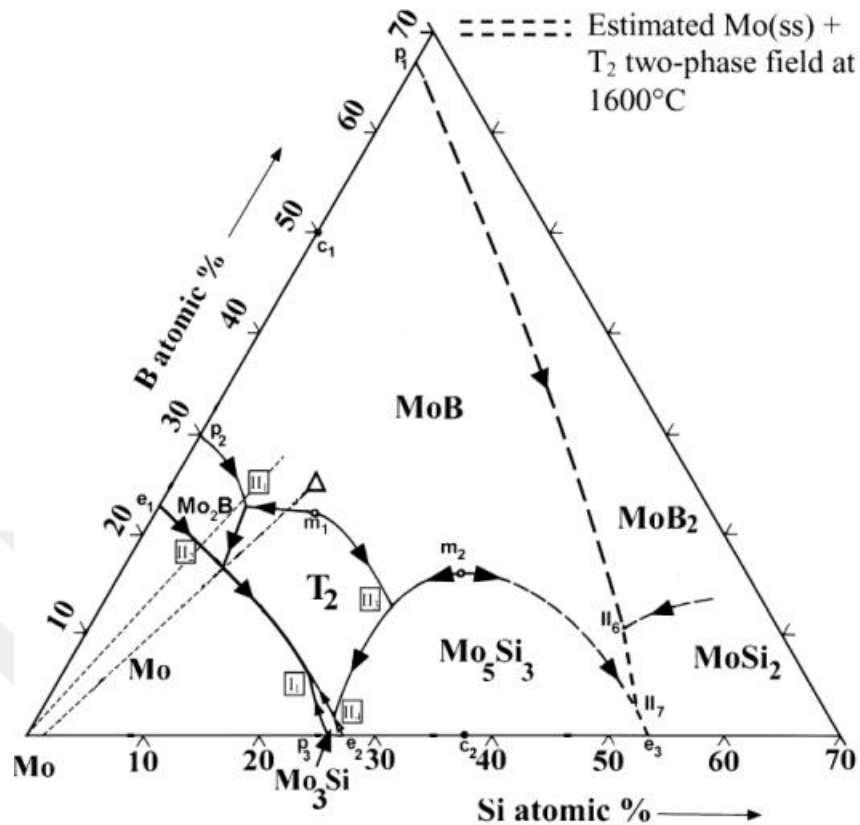


Figure 4.1. The MoSiB phase diagram showing the liquidus projection for the Mo-rich area, with the various zones of primary solidification highlighted (Nunes et al., 2018). In point II, we can see the Moss-A15-T2 invariant eutectic. (C.A. Nunes, 2000)

Representative micrographs of three phase alloys prepared by Nunes et al. using arc melting process are shown in Figure 4.2 for the as cast condition.

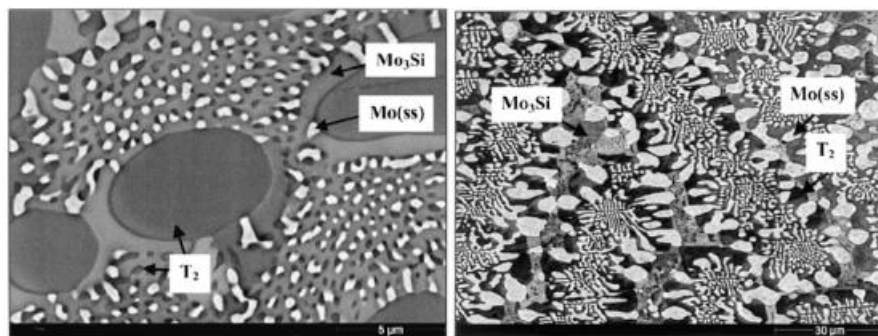


Figure 4.2. Two arc-melted alloys, Mo-13Si-15B and Mo-9.6Si-14.2B, were imaged using BSE in their as-cast form (C.A. Nunes, 2000). Note the images are shown at different magnifications

4.2. Hot Working

Some researchers have successfully processed alloys with higher molybdenum contents. Berczik employed rapid solidification and hot working, as outlined in his patents, to fabricate two-phase Moss T2 alloys characterized by a dispersion of T2

particles within a continuous molybdenum matrix. This method enhances the microstructure and mechanical properties of the alloys by promoting a more uniform distribution of intermetallic phases within the ductile molybdenum matrix, Figure 4.3 (Patent No. 5,595,616, 1997), (Patent No. 5,693,156, 1997). The alloy experienced rapid solidification by a splat quenching method, yielding a high cooling rate that enabled the formation of a supersaturated molybdenum solid solution. The powdered material was subsequently placed in a vacuum-sealed molybdenum container and subjected to extrusion and swaging processes for consolidation. Subsequently, thermal treatments were employed to control the precipitation of the T2 intermetallic phase from the supersaturated solution. This approach guarantees uniform and consistent dispersion of T2 particles inside the continuous molybdenum matrix, hence improving the mechanical properties and oxidation resistance of the alloy.

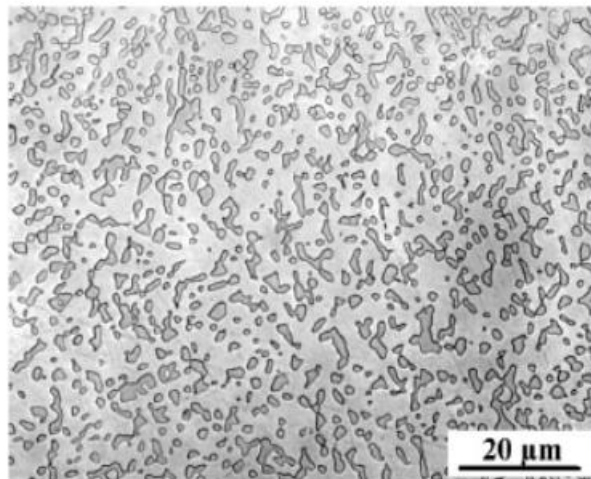


Figure 4.3. Pratt & Whitney (East Hartford, CT) developed a Moss-T2 alloy that had a continuous molybdenum matrix. Extrusion was used to solidify a super-saturated Moss powder that had been rapidly solidified. Separate dispersoids of T2 were precipitated from a Moss matrix by means of a controlled heat treatment. (P. Jéhanno M. H., 2004)

4.3. Powder Metallurgy

Berczik asserts that various powder processing techniques, such as cold isostatic pressing (CIP), sintering, hot isostatic pressing (HIP), and field-assisted sintering techniques (FAST), can be employed to achieve an optimal microstructure. These methodologies affect the microstructural characteristics by altering process parameters, facilitating a multi-step near-net-shape production procedure. Nonetheless, these methods are vulnerable to embrittlement induced by oxygen contamination. Consequently, it is imperative to meticulously monitor the manufacturing environment and effectively

eliminate all sources of oxygen to prevent embrittlement and maintain the desired mechanical properties in the final alloy. Hot worked MoSiB alloys have been successfully employed to produce microstructures with distributed intermetallic phases in a molybdenum-based main phase, but the methods involved are frequently challenging and costly. The powders were mixed in inert atmosphere and hot pressed at 1650°C, followed by annealing for homogenize the microstructures, as shown in, Figure 4.4. The resulting alloy exhibited a fine grain structure; however, the molybdenum phase lacked continuity. High carbon levels were introduced from the graphite dies utilized during hot pressing, while a notable proportion of silicate inclusions formed due to elevated oxygen impurities. These contaminants negatively impacted the alloy's microstructure and properties, underscoring the critical need for contamination control throughout the powder metallurgy process.

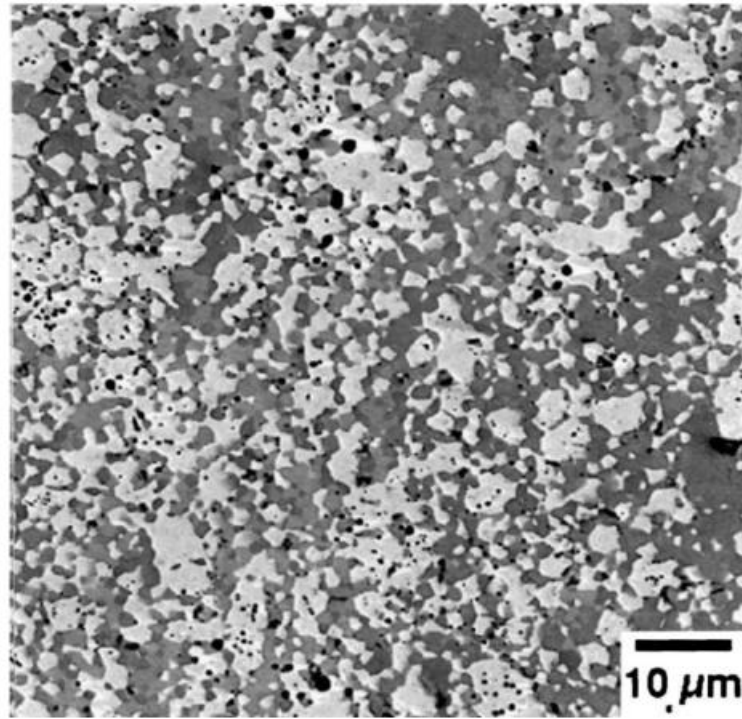


Figure 4.4. A BSE micrograph depicting a Mo-9.4Si-13.8B at.% alloy, meticulously prepared by Nieh *et al.* through the hot pressing of elemental powders of molybdenum, silicon, and boron. The dark areas present in the image represent silica inclusions. (T.G. Nieh, 2001)

A significant issue associated with the previously stated powder metallurgical procedures is the elevated residual oxygen concentration. The primary materials are susceptible to oxidation, and the processing of tiny powders intensifies this issue. The surface oxidation of silicon, boron, and molybdenum silicides is notably challenging to regulate and persists in the sintered alloys. Schneibel *et al.* demonstrated that their alloys

possess markedly reduced oxygen levels in comparison to those fabricated by Liu et al. This discrepancy mostly stems from Liu et al.'s use of coarser powders, which have a reduced surface area and are hence less susceptible to oxidation. This study emphasizes the essential significance of choosing appropriate particle sizes and processing parameters to minimize oxygen contamination and enhance the overall quality of the final alloy.



5. EXPERIMENTAL WORK

The experimental procedures and equipment used to prepare and characterize SiC whisker added MoSiB alloys produced via spark plasma sintering are introduced in the following chapter. Various percentages of SiC whisker additions were employed to investigate their effects on the microstructure and mechanical properties of the alloys.

The characterization techniques employed include:

- X-ray diffraction (XRD),
- Scanning electron microscopy (SEM),
- Electron backscatter diffraction imaging (EBSD).

The analytical methods used to interpret the microstructural parameters are also detailed. These methods are crucial for understanding how the addition of SiC whiskers influences the structural and mechanical characteristics of the MoSiB alloys.

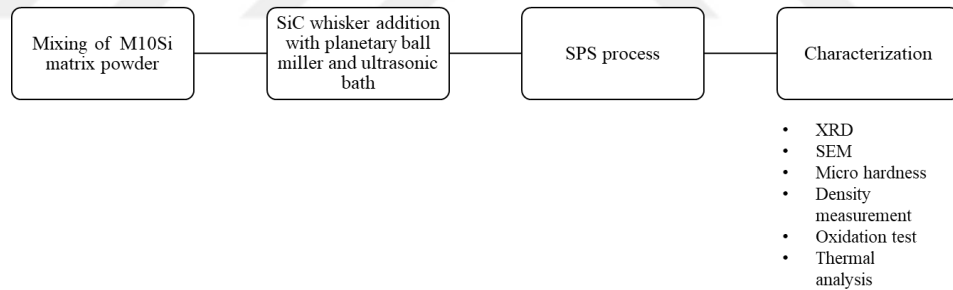


Figure 5.1. Schematic figure of experimental procedure

5.1. Selection Of Composition

The alloy composition profoundly impacts the resulting microstructure and characteristic properties. The addition of silicon (Si) and boron (B) to molybdenum (Mo) alloys not only facilitates the formation of secondary phases but also involves dissolution in the Moss phase. This interaction significantly influences the alloys' fracture toughness, ductility, strength, and density. For this research, the M10Si matrix composition was selected as the base. SiC whiskers were added as weight percent (% wt) and atomic percent (%at) variations over this base composition.

5.2. Preparation Of Powder Mixture

Molybdenum is predominantly used as an additive to strengthen steel and trademark nickel based superalloys. Typically, it is added in its molten form, and only a limited number of suppliers produce molybdenum powder suitable for powder metallurgy. This requires a delicate, unagglomerated powder that can sinter effectively at reasonable temperatures.

In this study, we utilized Ultrafine grade molybdenum powder from Nanografi. The selection of this powder, with a particle size of 1 μm , was based on a rigorous process that considered factors such as high purity and low oxygen content. The impurity levels of the powders were provided by the manufacturers. A list of the powders used and an overview of their properties are detailed in the study.

Table 5.1. *Experimental powder properties*

Raw Material	Purity (%)	Particle Size (μm)	Supplier
Mo	99.99	1	Nanografi
Si	99.99	1	Nanografi
B	99+	5	Nanografi
SiCw	99.99	0.65 (diameter)	Haydale

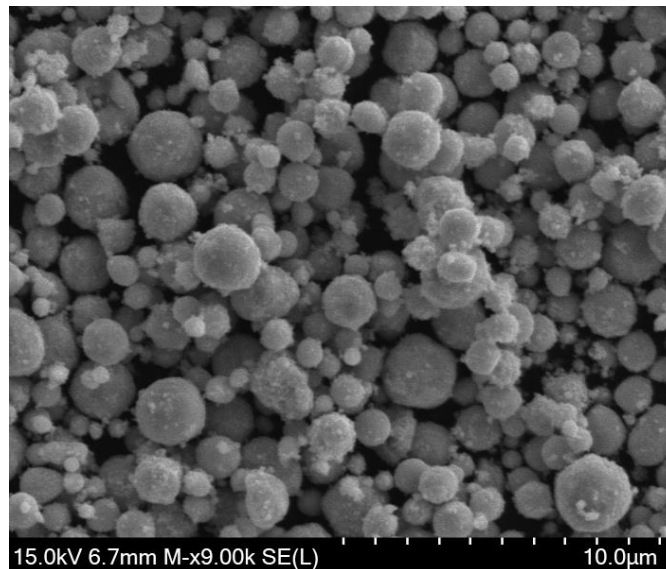


Figure 5.2. *SEM images of Mo powder*

The crystalline boron powder used in the study was produced by Nanografi, with a reported d50 particle size of 1 μm . However, it was noted that the powders were agglomerated. An SEM micrograph of the crystalline B powder is shown in Figure 5.3.

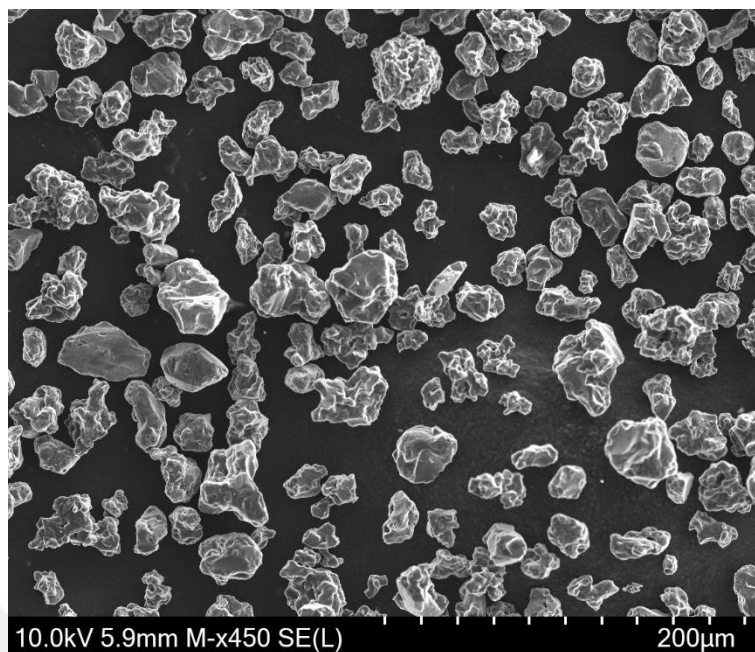


Figure 5.3. SEM images of crystalline B powder

Silicon whisker powders used in different size distributions were purchased from Haydale. Initially, examined with an average diameter size of approximately 0.65 μm . SEM images of the powders are shown in Figure 5.4.

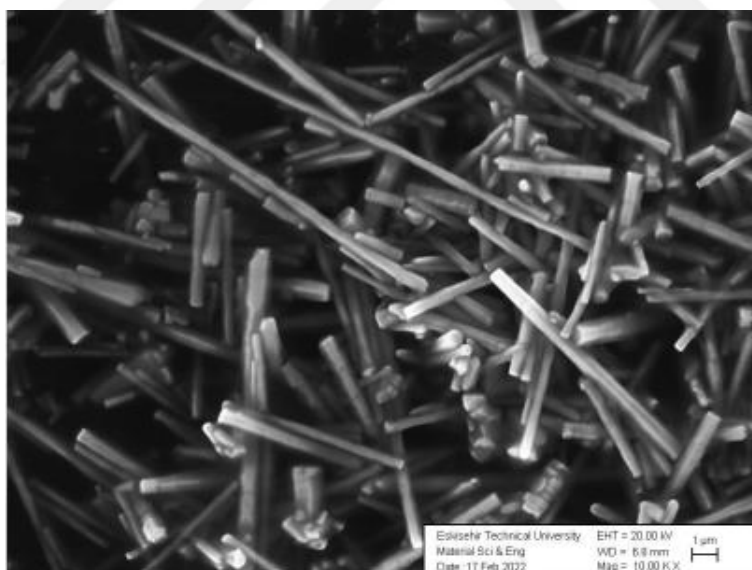


Figure 5.4. SEM images of crystalline SiC whisker

For alloying, the powders of Mo (purity 99.99%), Si (>99.99%), B (99.9%), and SiC whiskers (purity 99%) were weighed and mixed under a non-protective atmosphere. The subsequent step of mechanical alloying was performed in a planetary ball mill (Fritsch Pulverisette 6), as shown in Figure 5.5(a). This apparatus facilitates a more efficient energy transfer relative to other conventional milling components, such as

attritors or vibrating mills. This mechanical alloying process, referred to as high-energy milling, is characterized by the superposition of centrifugal and Coriolis forces, incorporating many phases of motion such as rolling (cascade movement), falling (cataract movement), and the centrifuging of balls. The influence of balls and supplementary friction during the cataract motion produces the maximum energy transfer, establishing them as the primary processes for mechanical alloying. This procedure entails the repetitive fracturing and rejoining of powder particles, leading to atomic-level homogenization.



Figure 5.5. Planetary ball mill (a) and (b) schematic of cataract movement during milling

Therefore, the powder mixtures were placed into grinding tools containing ZrO_2 balls ($d = 10$ mm) at a powder to ball ratio of 1:1. These closed grinding tools were then secured within a planetary ball mill, operating at rotational speeds of 200 rpm and 300 rpm for durations of 1 hour and 2 hours, respectively.

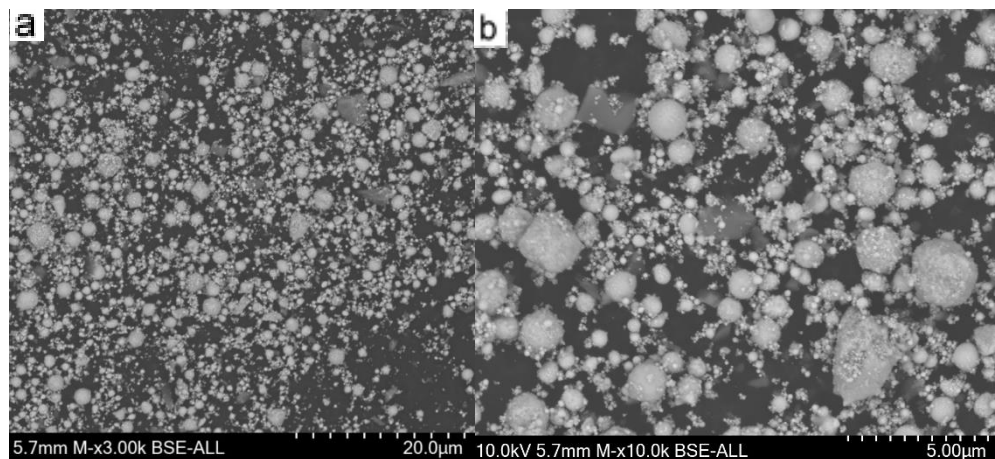


Figure 5.6. a) BSE images of 3000x magnification and b) BSE images of 10000x magnification M10Si matrix powder

To achieve a homogeneous distribution of the SiC whiskers, which are used to enhance hardness and fracture toughness values, the powder mixture and whisker material

were dispersed uniformly in a structure using an ultrasonic bath before initiating the ball milling process.

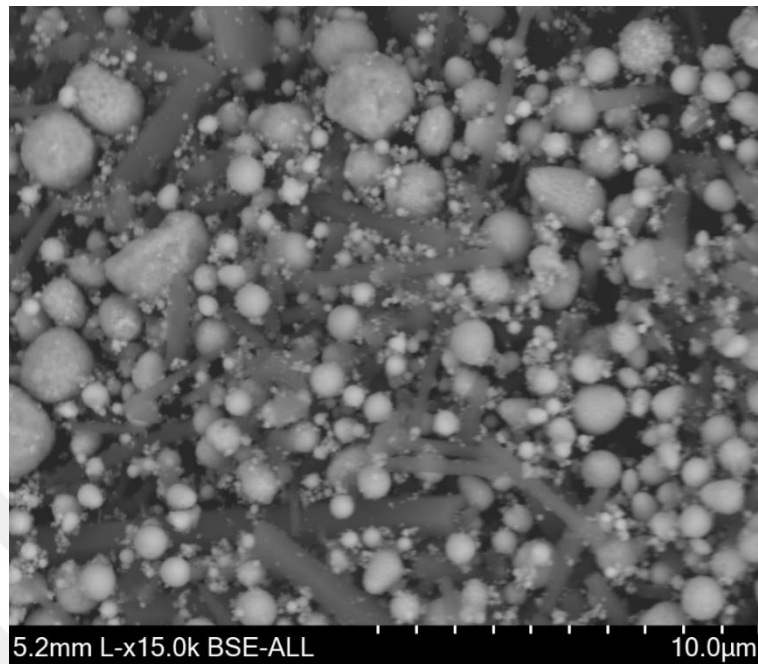


Figure 5.7. BSE images of $M5SiC_{20}$ powder mixture

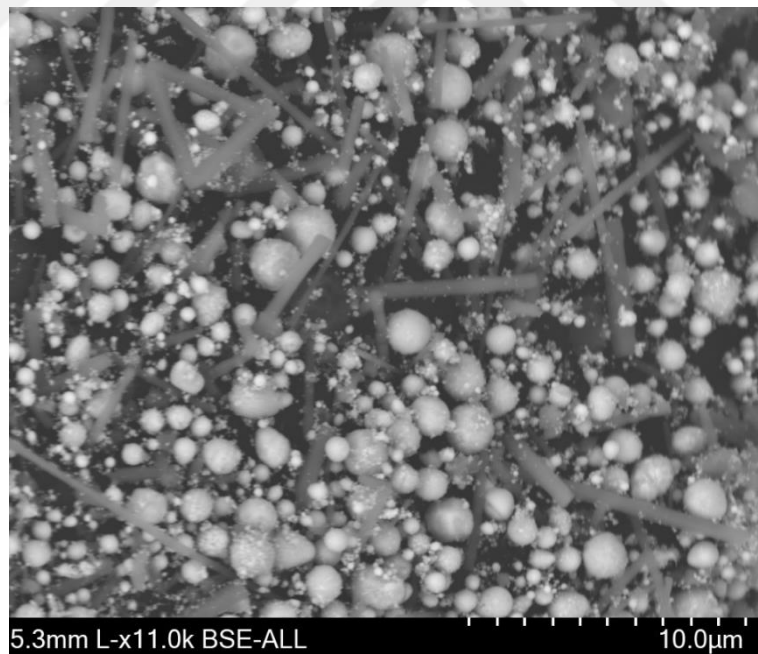


Figure 5.8. BSE images of $M3.3SiC_{15}$ powder mixture

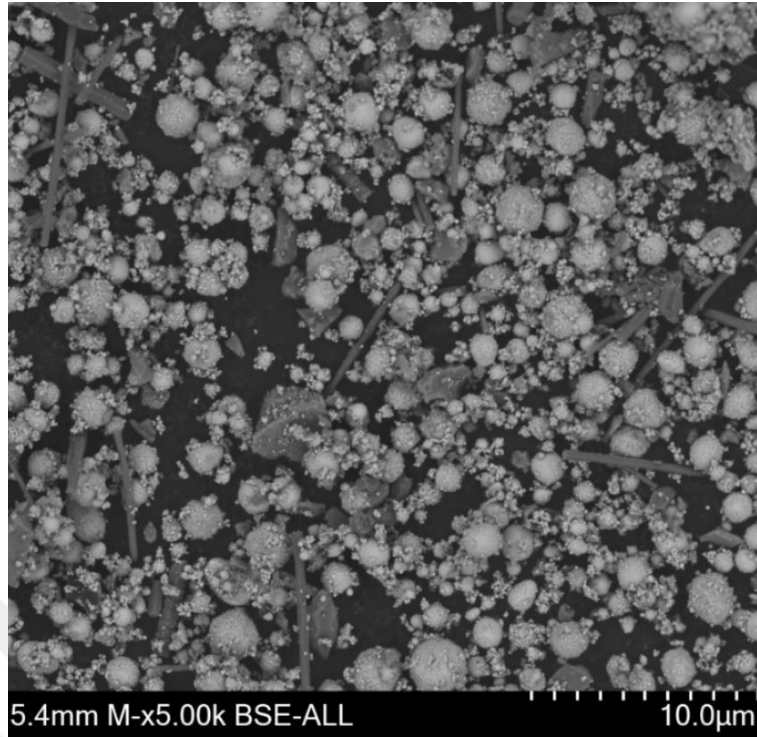


Figure 5.9. *BSE images of M10SiC2 powder mixture*

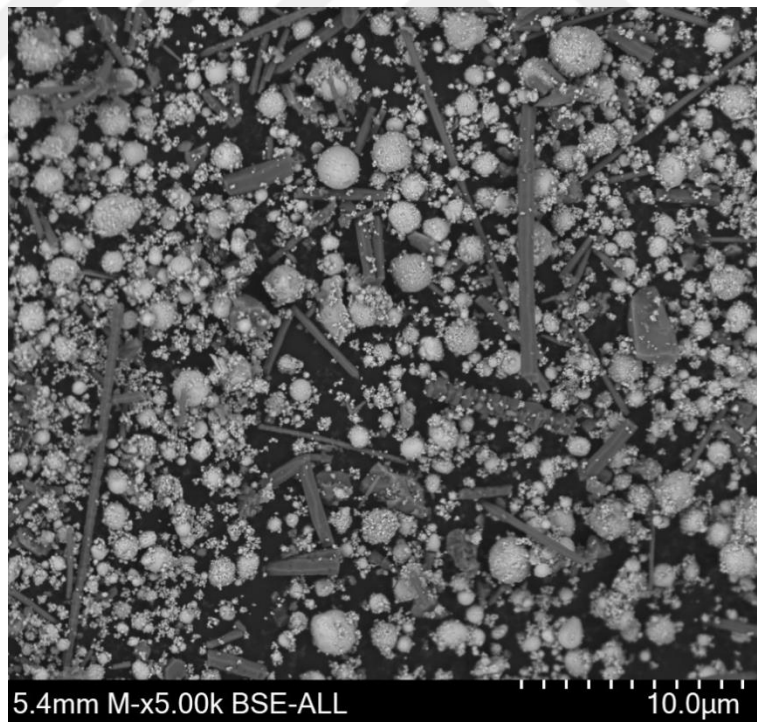


Figure 5.10. *BSE images of M10SiC5 powder mixture*

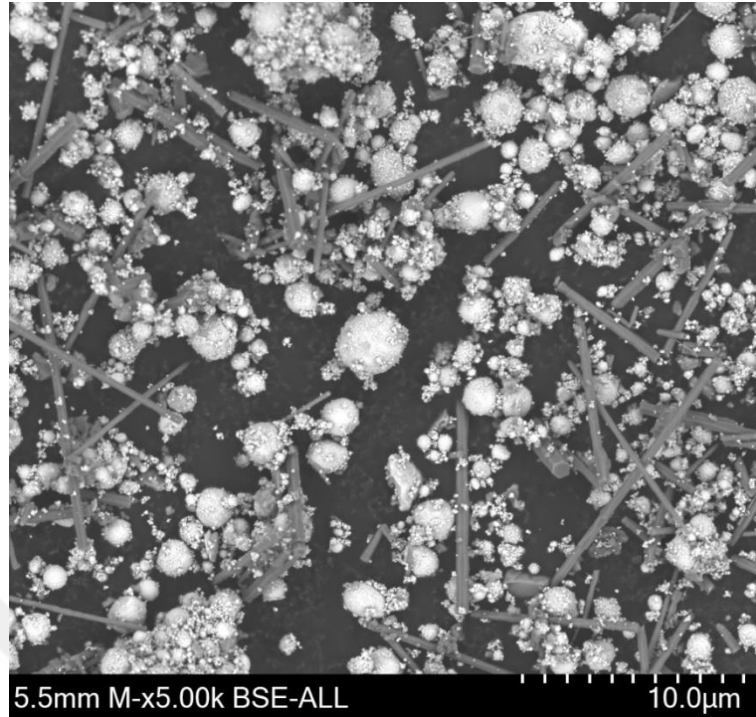


Figure 5.11. BSE images of M10SiC8 powder mixture

5.3. Spark Plasma Sintering Procedure

Spark Plasma Sintering (SPS) typically refers to a technique that involves applying simultaneous uniaxial pressure and low voltage pulsed current, as illustrated in Figure 5.12. SPS might be considered a kind of hot pressing, in which the traditional furnace is replaced by a mold containing the sample, heated directly by the current flowing through it and subsequently through the sample itself. Nevertheless, a definitive and universally accepted definition of SPS and its associated procedures remains elusive due to varying interpretations and methodologies.

The term "SPS" has sparked criticism, as the presence of plasma and electric discharges throughout the process has not been conclusively shown despite numerous attempts. Over the past two decades, SPS has garnered increased attention due to its remarkable efficiency, enabling fast sintering and densification, particularly for materials that are difficult to sinter, such as highly refractory materials, metastable phases, or nanomaterials. SPS has emerged as the preferred sintering technique for various high-temperature materials.

In contrast to traditional sintering methods including pressureless sintering, hot pressing, and hot isostatic pressing, Spark Plasma Sintering (SPS) possesses some unique characteristics. These encompass accelerated heating rates, abbreviated sintering durations, diminished sintering temperatures, and minimized grain development. SPS

systems generally attain heating speeds of several hundred degrees per minute, with the potential to exceed 1000°C per minute. These values exceed those in conventional sintering processes by one to three orders of magnitude, facilitating substantial reductions in sintering cycle lengths.

In addition to accelerated heating rates, SPS facilitates reduced overall sintering durations. The synergistic impact of accelerated heating and abbreviated cycles can diminish standard sintering times from hours to only minutes, starkly contrasting with the extended durations necessitated by traditional sintering methods. Furthermore, SPS's improved efficiency enables reduced sintering temperatures, frequently by several hundred degrees Celsius, which is especially advantageous for very refractory materials. Decreased sintering temperatures lead to decreased grain development, yielding materials with smaller grain sizes and enhanced mechanical characteristics.

Thus, SPS offers significant advantages in speed, temperature efficiency, and final material properties compared to traditional sintering methods. In this study, powder mixtures are weighed in 13 gram batches and placed in 10 mm diameter graphite SPS molds. The SPS process parameters and sample codes are listed in Table 5.2.

Table 5.2. (Continued) Process parameters of SPS

Sample Codes	Alloy Composition	Addition of SiCw	SPS Parameters				
			Heating rate (°C/min)	Cooling rate (°C/min)	Maximum Temperature (°C)	Holding Time at Maximum Temperature (min)	Pressure (MPa)
M10Si	%at 80 Mo %at 10 Si %at 10 B	-	100	100	1600	30	40
M5SiC20	%at 65 Mo %at 5 Si %at 10 B	%at 20 SiCw	100	100	1600	10	12
M3.3SiC15	%at 20 SiCw %at 65 Mo %at 3.3 Si %at 6.7 B	%at 15 SiCw	100	100	1600	10	12
M10SiC2	%at 15 SiCw %at 80 Mo %at 10 Si %at 10 B % wt 2SiCw	%wt 2 SiCw	100	100	1600	30	40

Table 5.3. (Continued) Process parameters of SPS

M10SiC5	% at 80 Mo						
	% at 10 Si	% wt 5	100	100	1600	30	40
	% at 10 B	SiCw					
	% wt 5 SiCw						
M10SiC8	% at 80 Mo						
	% at 10 Si	% wt 8	100	100	1600	30	40
	% at 10 B	SiCw					
	% wt 8 SiCw						

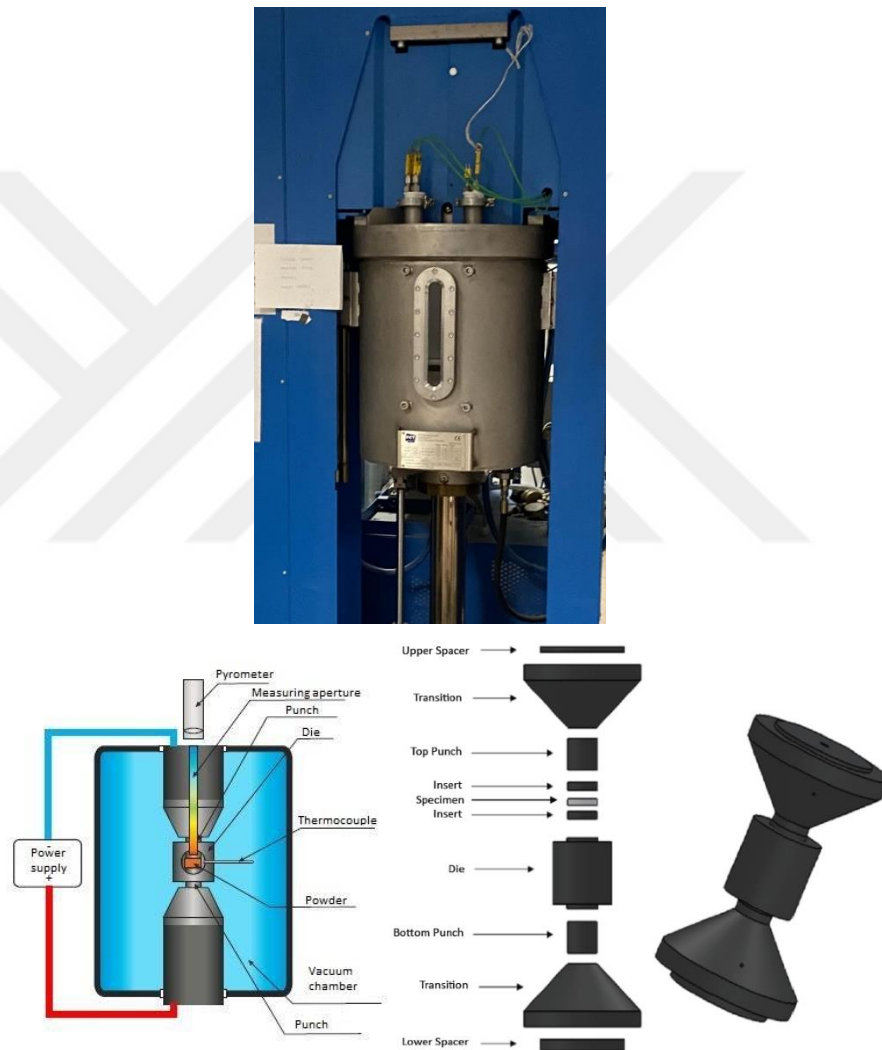


Figure 5.12. Setup for spark plasma sintering technology (SPS) at the Eskişehir Technical University (ESTÜ) Eskişehir, Turkey (a) structure of the SPS (b) schematic structure according to (c) SPS tooling design

A heating rate of 100°C/min and different holding durations at 1600°C, aligned with the isothermal temperature indicated on the ternary phase diagram, were utilized for processing. The procedure was performed under vacuum conditions ($P < 10$ Pa) and exposed to a uniaxial pressure of 9 MPa. Samples were prepared for analysis via scanning

electron microscopy (SEM) and subjected to thermomechanical evaluations. These processes were essential for evaluating the microstructural attributes and mechanical qualities of the materials produced under these particular conditions.



6. EXPERIMENTAL RESULTS

Various techniques were employed to characterize the materials, study the reactions involved in forming the intermetallic phases, and investigate the impact of sintering parameters on the distribution of phases in the alloys. These techniques used in this work typically included:

1. Microstructural Analysis: Using technique Hitachi SU5000 trademark scanning electron microscopy (SEM) to examine phase size, shape, and distribution.

2. Phase Analysis: Utilizing Rigaku Rint 2000 trademark X-ray diffraction (XRD) to identify the crystalline phases present in the alloys.

3. Chemical Analysis: Hitachi SU5000 trademark energy-dispersive X-ray spectroscopy (EDS) is employed to determine the elemental composition and distribution within the phases.

4. Mechanical Testing: Conduct tests such as Vickers hardness testing and Evans-Charles Equation fracture toughness measurements to evaluate mechanical properties.

5. Thermal Analysis: Performing NETZSCH STA 449F3 trademark differential scanning calorimetry (DSC) or thermal gravimetric analysis (TGA) to study thermal behavior and phase transformations.

These characterization techniques collectively provide comprehensive insights into the alloys' composition, structure, and properties, enabling a detailed understanding of their behavior under different processing conditions.

6.1. Density Measurement

The densities of the samples were measured using the Archimedes method. The densities of the materials are based on Mo, Si, B and SiC whisker; 10,21 g/cm³, 2,32 g/cm³, 2,3 g/cm³ and 3,2 g/cm³ respectively.

Density calculations of post-process samples were performed based on the intermetallic phases present. The volumes of the phases were determined from the isothermal MoSiB ternary phase diagram at 1600°C. The volume fractions were assumed to be constant across a wide temperature range, as this phase region is known to be stable down to room temperature (Dimiduk, 2003). In calculating the phase ratios, it is assumed that all the boron resides exclusively in the T2 phase. This assumption stems from the understanding that boron shows negligible solubility in molybdenum at temperatures up to 1600°C, as indicated by the molybdenum-boron binary phase diagram. Therefore, any boron in the alloy is directly proportional to the amount of the T2 phase that forms. This

approach is grounded in understanding phase equilibria and helps accurately determine the composition and distribution of phases in MoSiB alloys (Hansen, 1958). It is also known that there is little solubility of boron in the A15 phase. Recognizing that little silicon goes into solution in the molybdenum phase, the remaining silicon available to form the A15 phase can be determined (Hansen, 1958). To calculate the composite density, considering the densities provided:

- A15 phase density = 8.98 g/cm³
- T2 phase density = 8.76 g/cm³
- T1 phase density = 8.19 g/cm³ (provided separately)

Given that the composite material's A15 and T2 phases are present, their densities are weighted according to their volume fractions. The average density of the intermetallics (A15 and T2) was provided as 8.9 g/cm³.

To find the composite density, which includes both the intermetallic phases (A15 and T2) and the T1 phase, we calculate it as follows:

$$d_{MoSiB} = 10,21 * V_f(Mo_{SS}) + 8,9 * 1 - V_f(Mo_{SS}) \text{ rely on Berczik triangle phases}$$

$$d_{MoSiB} = 8,9 * V_f(Mo_5Si_3) + 8,3 * 1 - V_f(Mo_5Si_3) \text{ rely on Akinc triangle phases}$$

As can be seen in the Figure, there are three intermetallic phases expected to occur at 1600 °C. These are Mo_{SS}, Mo₃Si (A15), Mo₅SiB₂ (T2) and Mo₅Si₃ (T1) phases. The percentages of these intermetallic are important for the main composition that will be formed after the sintering process.

Table 6.1. Density values for all samples

Sample Codes	Bulk Density (g/cm ³)	Theoretical Density (g/cm ³)	Open Porosity (%)
M10Si	7,81	9,62	18,81
M5SiC20	7,10	8,66	18,01
M3.3SiC15	7,46	8,37	14,45
M10SiC2	7,37	9,62	22,09
M10SiC5	7,31	9,62	22,72
M10SiC8	7,25	9,62	23,36

Fabricating MoSiB alloys through powder metallurgy offers significant advantages over melt-based processing, such as eliminating non-equilibrium phases and achieving finer microstructures. However, several challenges specific to powder processing must be addressed for successful production:

1. **Impurity Control:** Ensuring high purity of raw materials is crucial to minimize impurities in the final alloy, which can affect its properties and performance.
2. **Porosity:** Minimizing residual porosity in the sintered alloys is essential for achieving desired mechanical properties and structural integrity.
3. **Scalability:** It is critical to develop production techniques that are scalable to industrial volumes. Processes must be robust enough to maintain quality and yield consistently at larger scales beyond laboratory experiments.
4. **Process Optimization:** Optimizing the powder metallurgy process parameters (such as particle size, compaction pressure, sintering temperature, and time) to achieve the desired microstructure and properties without introducing defects or compromising material integrity.
5. **Cost Considerations:** Balancing the costs associated with raw materials, processing, and equipment with the alloy's performance requirements.

Addressing these issues involves a combination of material science, process engineering, and industrial-scale manufacturing considerations to realize the full potential of MoSiB alloys in practical applications.

In the literature, hot isostatically pressed (HIPped) sample encapsulation has been noted as necessary due to significant open porosity. While some residual porosity remains even after HIPping, achieving total density may be possible with adjustments such as higher temperatures, increased pressures, or longer hold times during sintering. Optimizing sintering parameters is crucial for MoSiB alloys to minimize porosity and achieve desired material properties. It involves carefully adjusting factors such as sintering temperature, pressure, and duration to promote densification without compromising the microstructure or introducing defects.

6.2. Phase And Microstructure Analysis

XRD patterns of starting powders patterns are given in Figure 6.1, Figure 6.2 and Figure 6.3, Figure 6.4 . XRD diffraction patterns, any data on the presence of secondary or amorphous phases. In addition, there is no ZrO₂ contamination which is for material used during the milling process.

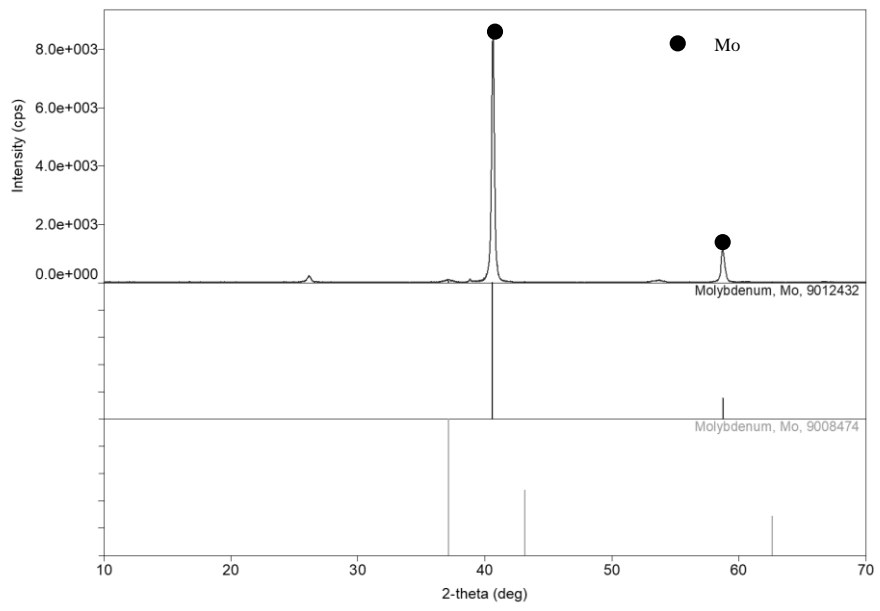


Figure 6.1. XRD pattern of the pure Mo

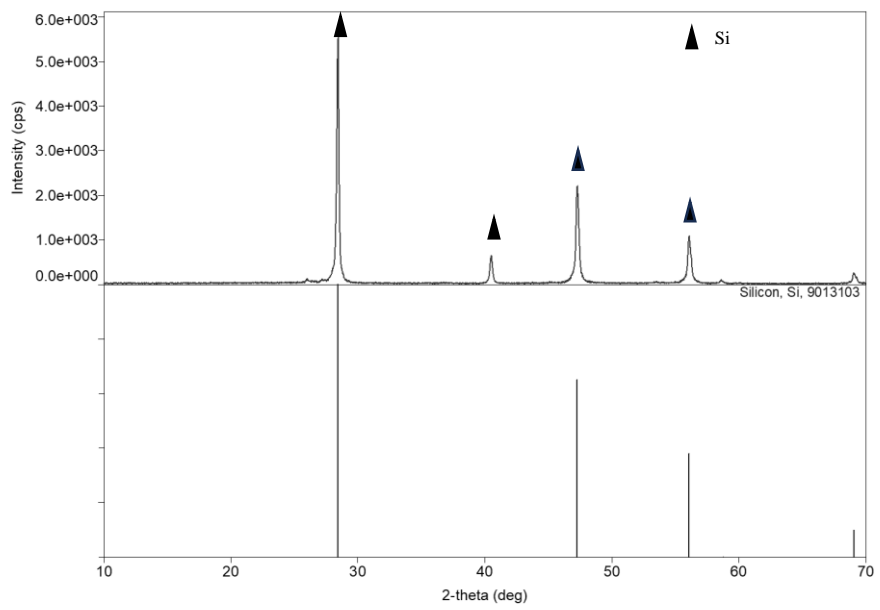


Figure 6.2. XRD pattern of the pure Si

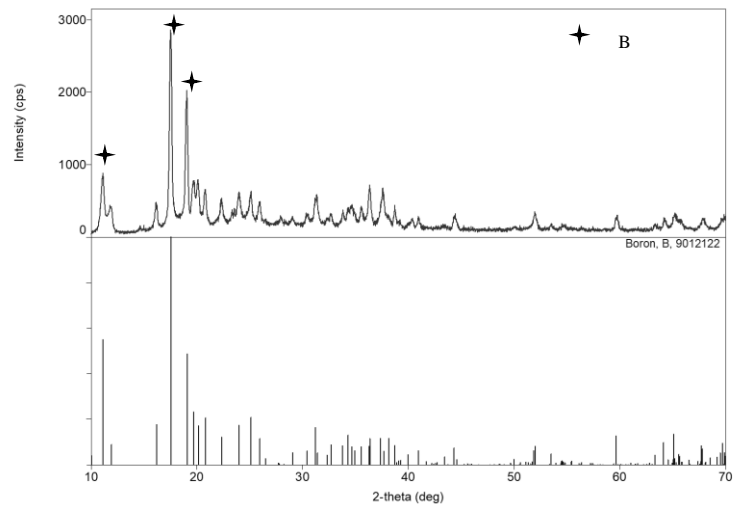


Figure 6.3. XRD pattern of the pure B

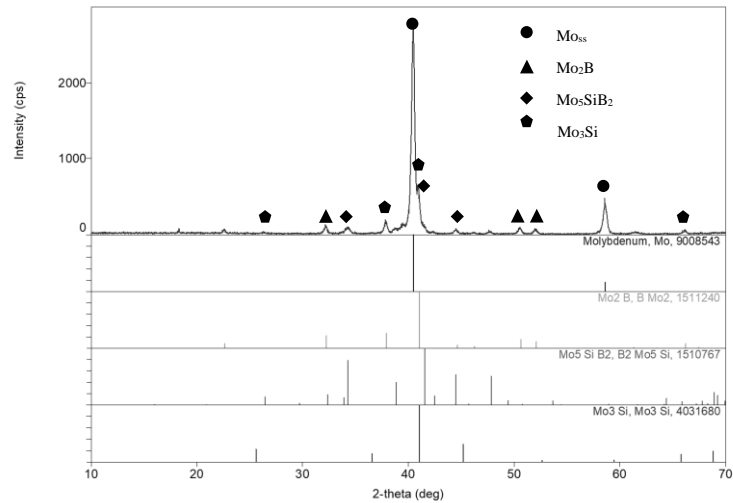


Figure 6.4. XRD pattern of the M10Si

Specimens underwent metallographic preparation stages, utilizing backscattered and variable electron modes to prevent sample surface charging. Images were captured at consistent magnifications (x1000, x3000, x5000, etc.) to facilitate comparison. No etching solution was applied to any of these samples.

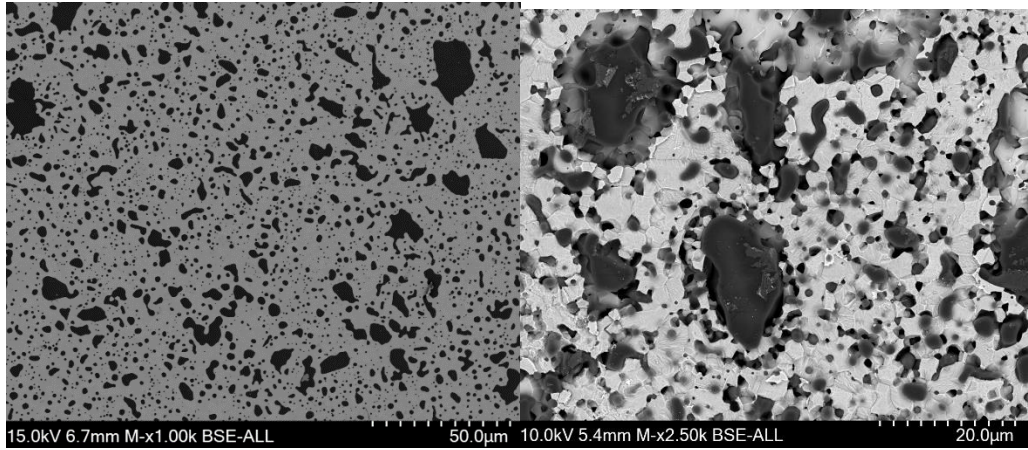


Figure 6.5. BSE images of M10Si SPSed sample

The alloy has that molybdenum phase does not appear continuous. The reason for that there was a high level of carbon from the graphite dies used for spark plasma sintering and a significant fraction of silicate inclusions were created due to high levels of oxygen impurities can be seen in Figure 6.5.

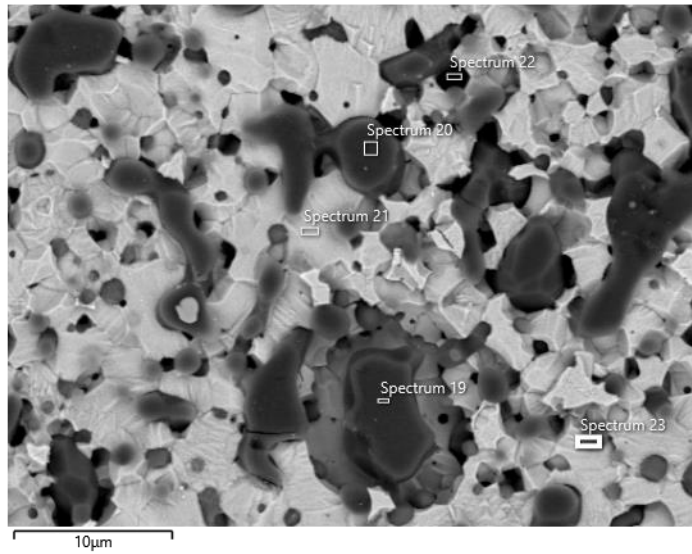


Figure 6.6. SEM-EDS spectrum analysis of M10Si SPSed sample

According to Figure 6.6 in the images white colored regions represent the Mo_{ss} phase because of the high atomic number of the phase and that the Mo_{ss} phase appears brighter than the intermetallic phases, gray regions represent the intermetallic A15 phase and dark phases represent the T2 phase.

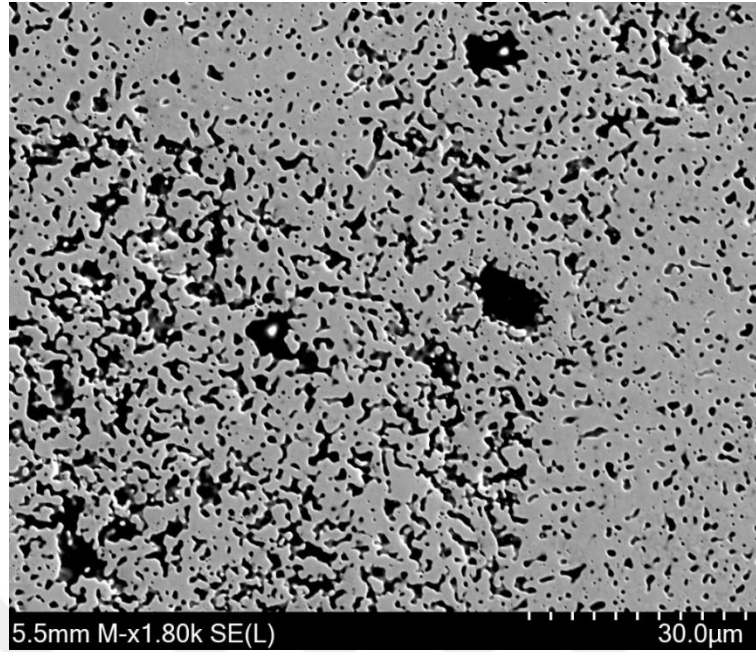


Figure 6.7. SEM-EDS spectrum analysis of M10Si SPSed sample

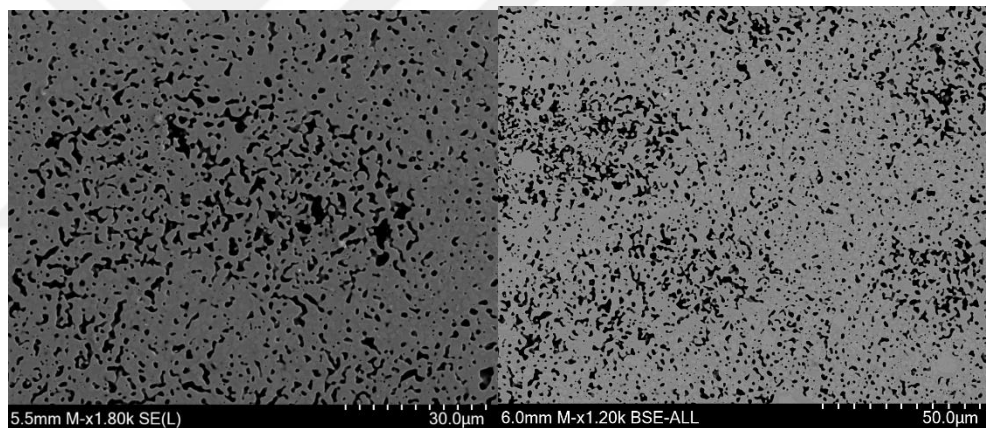


Figure 6.8. SEM images of M5SiC20 SPSed sample

It was determined that SiC whisker additives added as at% created macro-sized porosity in the sintered structures. It was also found that the whiskers were not homogeneously distributed in the sintered M5SiC20 sample can be seen that Figure 6.9.

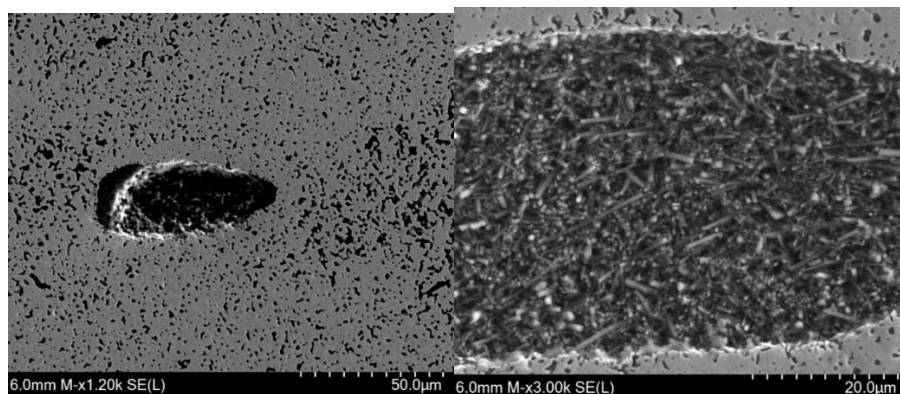


Figure 6.9. SEM images of containing non-homogenous SiC whisker M5SiC20 SPSed sample

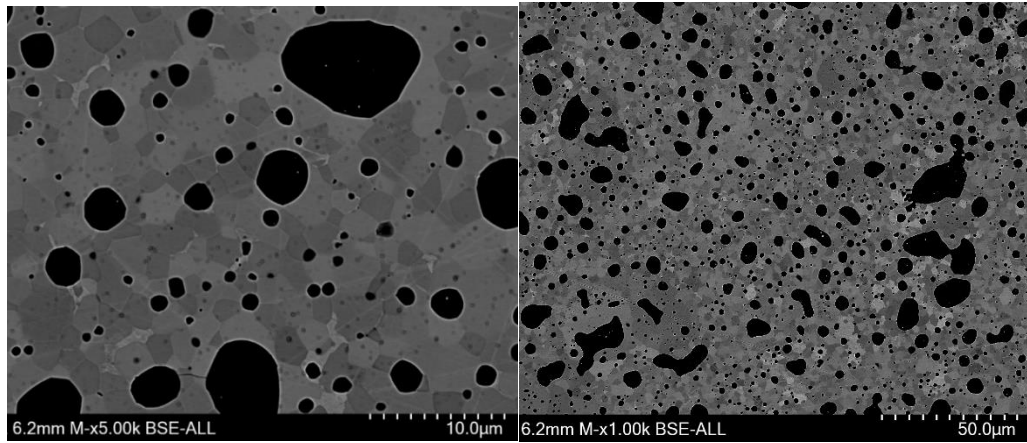


Figure 6.10. BSE images of M10SiC2 SPSed sample

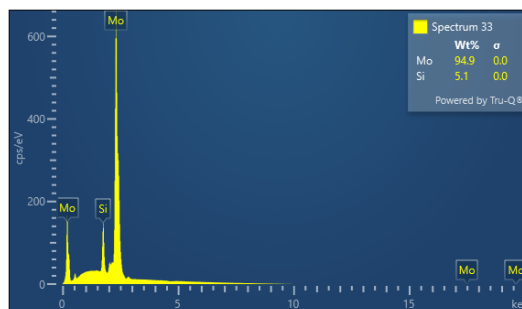
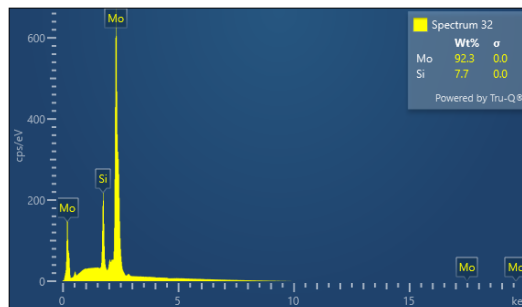
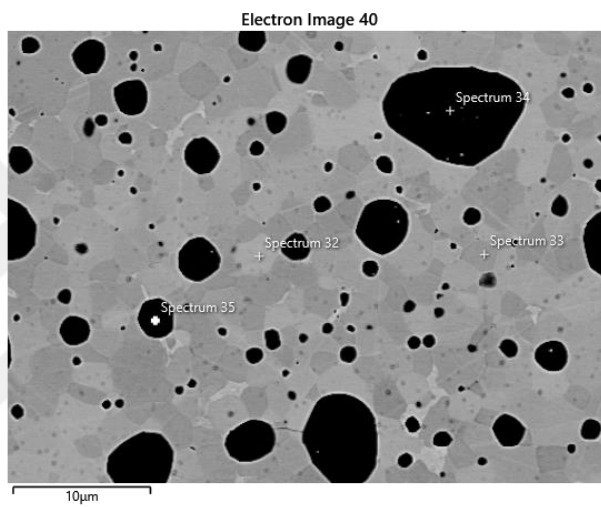


Figure 6.11. (Continued) SEM-EDS spectrum analysis of M10SiC2 SPSed sample

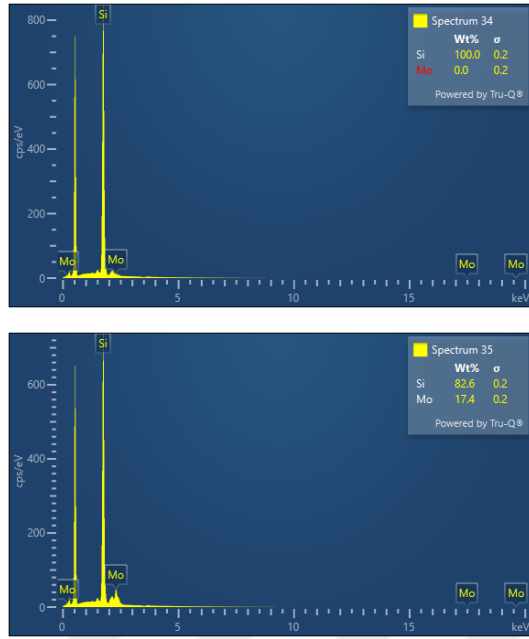


Figure 6.12. (Continued) SEM-EDS spectrum analysis of M10SiC2 SPSed sample

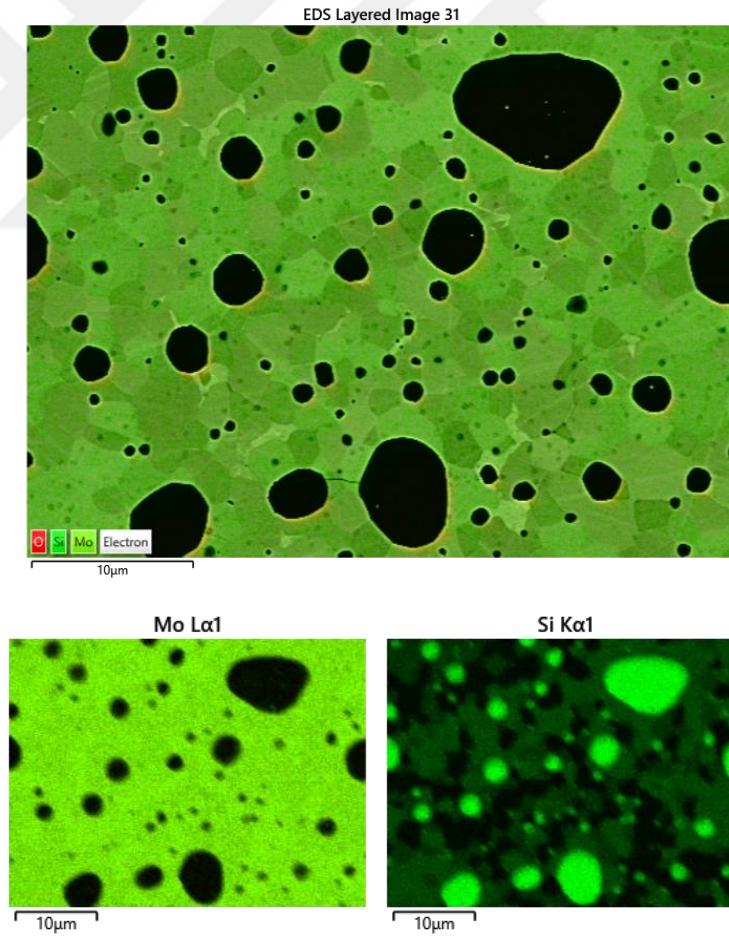


Figure 6.13. (Continued) SEM-EDS mapping analysis of M10SiC2 SPSed sample

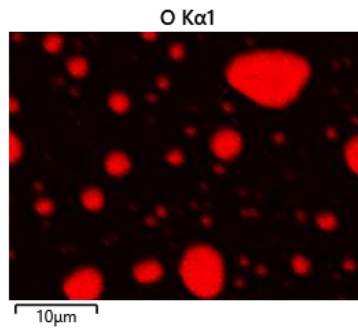


Figure 6.14. (Continued) SEM-EDS mapping analysis of M10SiC2 SPSed sample

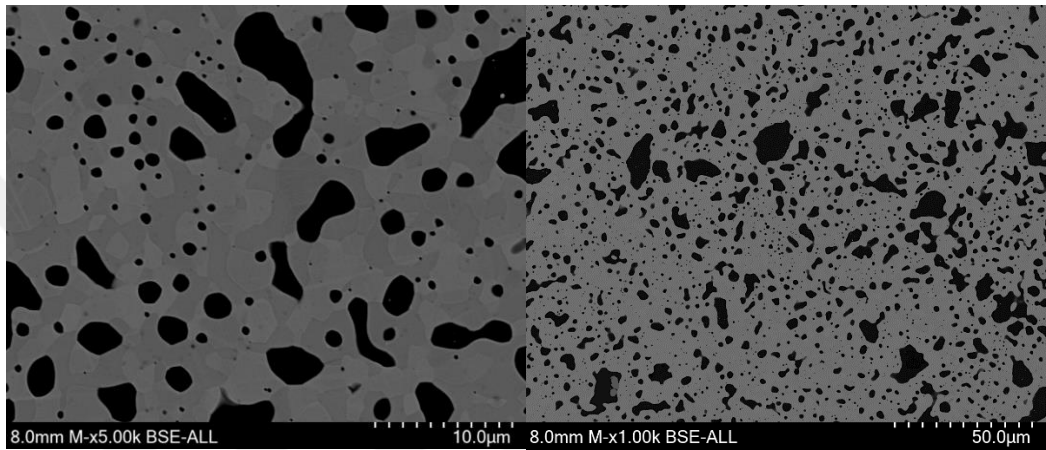


Figure 6.15. BSE images of M10SiC5 SPSed sample

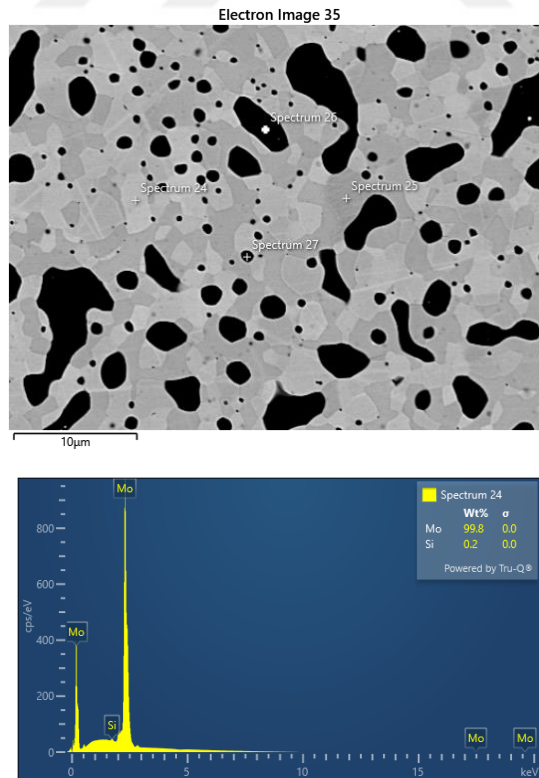


Figure 6.16. (Continued) SEM-EDS spectrum analysis of M10SiC5 SPSed sample

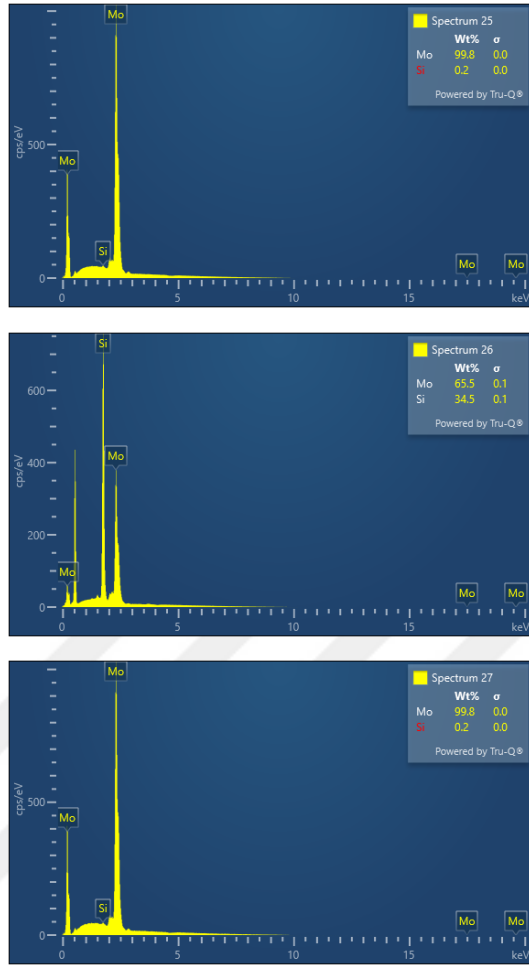


Figure 6.17. (Continued) SEM-EDS spectrum analysis of M10SiC5 SPSed sample

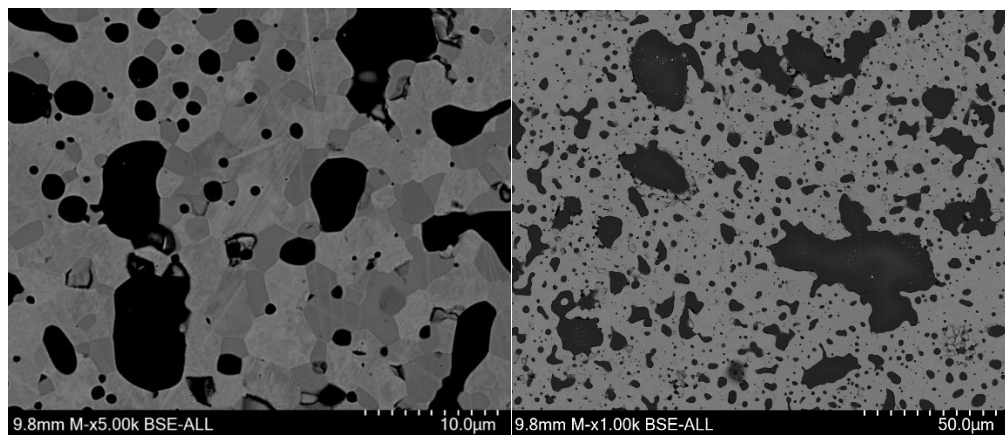


Figure 6.18. BSE images of M10SiC8 SPSed sample

6.3. Hardness And Fracture Toughness Measurement

Circular sintered samples were molded following metallographic processes. The surfaces of these sections were polished, and the hardness of the specimens was measured using the M1C model of EMCO-Test, employing the Vickers hardness measurement method. The hardness (HV) was determined under a 500 g load for 10 seconds, assessing

the crack lengths formed on the surface. Additionally, fracture toughness (K_{IC}) values were determined. Measurements were performed three times for each sample, and the averaged values were used.

The hardness of the materials was calculated using Equation 1, as given below:

$$Hv = \frac{0,47xF}{a^2}$$

(Equation 1)

H_v: Hardness of Vickers (GPa)

F: load (N)

a: half the diagonal length of the hardness indent trace (mm)

$$K_{IC} = 0,15H_v\sqrt{ak}\left(\frac{c}{a}\right)^{-3/2}$$

(Equation 2)

K_{IC}: fracture toughness (MPa.m^{1/2})

c: crack length

k: Correction factor (≈2,6)

a: half the diagonal length of the hardness indent trace (mm)

The c values obtained during the hardness measurements are calculated using Eq....

According to Evans-Charles equation, toughness values were also calculated:

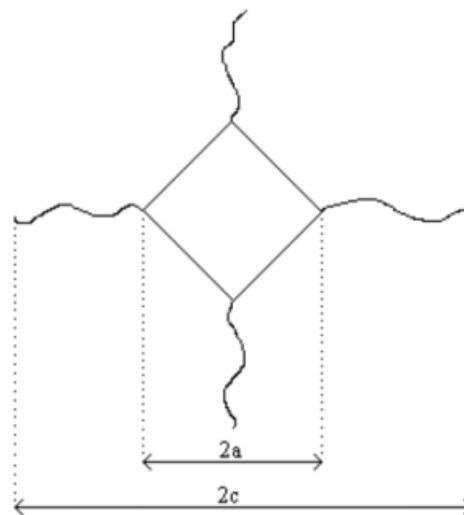


Figure 6.19. Schematic representation of the Vickers indent on the sample surface

As a result of the experimental studies, sintered by SPS method hardness and toughness measured because of applying 500 g load to the samples values are given in Table 6.2.

Table 6.2. *Hardness and fracture toughness value of all samples*

Sample Codes	Vickers Hardness (HV500 -GPa)	Fracture Toughness (MPa.m ^{1/2})
M10Si	4,95	-
M5SiC20	16,92	3,31
M3.3SiC15	18,10	1,97
M10SiC2	13,64	-
M10SiC5	12,01	-
M10SiC8	13,84	-

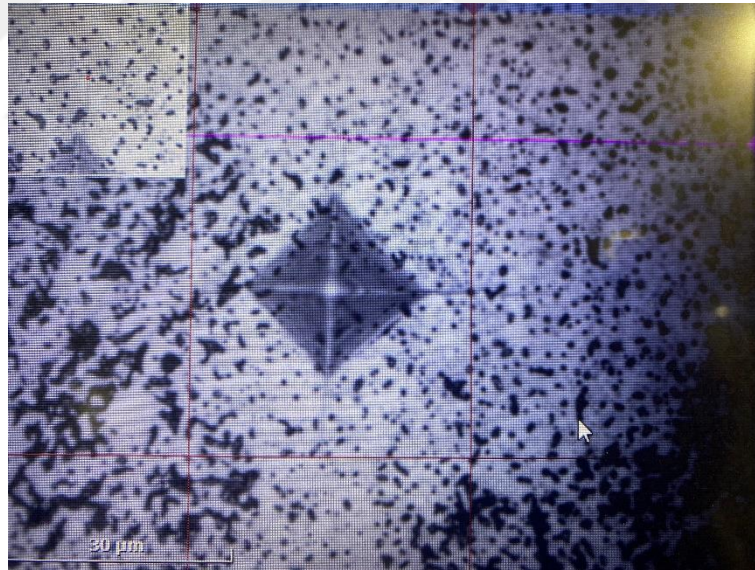


Figure 6.20. *Example of Vickers indentation image of M5SiC20*

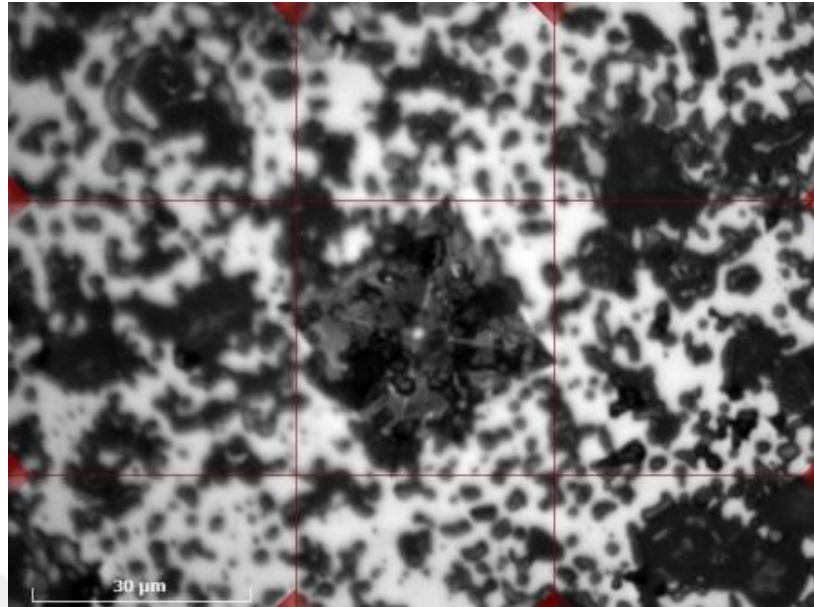


Figure 6.21. *Example of Vickers indentation image of M10SiC2*

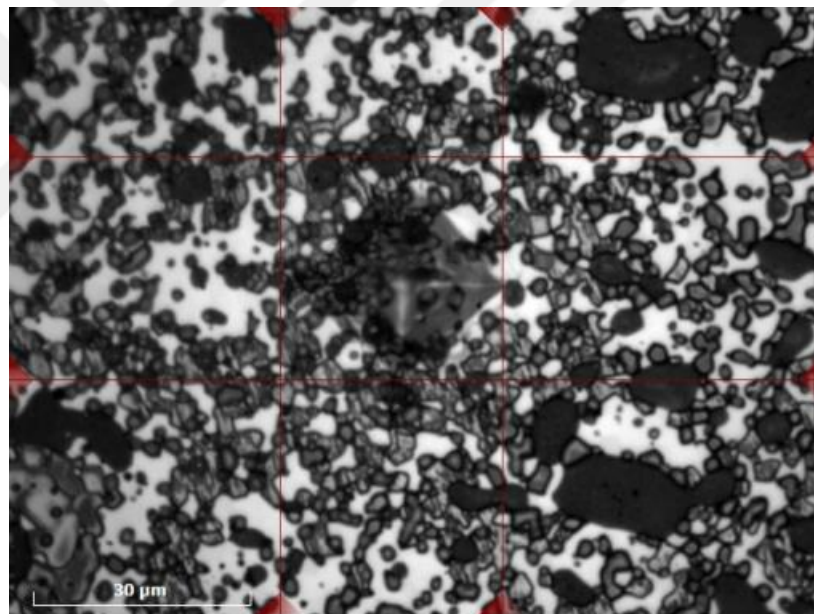


Figure 6.22. *Example of Vickers indentation image of M10SiC5*

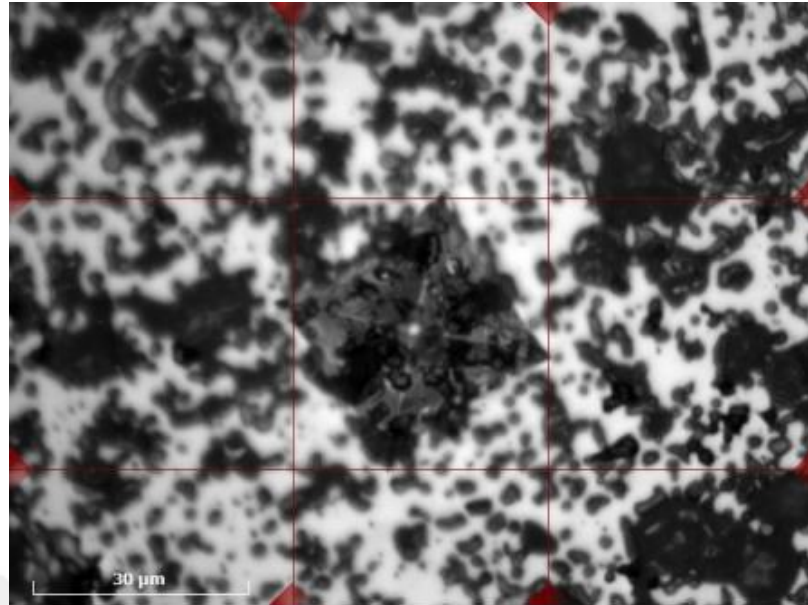


Figure 6.23. Example of Vickers indentation image of M10SiC8

Chu et al. utilized indent crack length measurements obtained from Vickers hardness indents to calculate the room temperature fracture toughness of Mo_5SiB_2 , an intermetallic material known for its brittleness. This method involves indenting the material with a Vickers hardness tester, then measuring the lengths of the cracks that emanate from the corners of the indent. These measurements provide critical data for calculating the material's fracture toughness, offering insights into the mechanical properties of Mo_5SiB_2 at room temperature (F. Chu, 1999). The determined value was $3.2 \text{ MPa}\sqrt{\text{m}}$; however, it is important to note that the analyzed samples comprised a three-phase intermetallic mixture of Mo_5SiB_2 , Mo_3Si , and a molybdenum boride phase, which may have affected the measurement. The inadequate fracture toughness of these intermetallic phases highlights the necessity of treating MoSiB alloys to enhance the distribution of A15 and T2 phases within a continuous molybdenum matrix. This method is essential for improving the comprehensive mechanical characteristics of the alloys. Enhancing the uniform distribution of these intermetallic phases can improve fracture toughness and other mechanical properties, rendering the alloys more appropriate for high-temperature and high-stress applications.

The indentation fracture toughness for M5SiC20 and M3.3SiC15 alloys could not be determined due to the absence of crack propagation in these specimens. The absence of crack propagation is likely related to the lack of damage-tolerance mechanisms in the material, probably resulting from the absence of the Moss phase in these particular

samples. The Moss phase enhances fracture toughness by mechanisms including crack trapping or bridging, potentially elucidating the observed behavior in certain alloys.

6.4. Oxidation Test

The oxidation resistance of the MoSiB alloys was assessed using oxidation experiments conducted at 1300°C for 6 hours in an atmospheric environment. The experiments were conducted utilizing alumina crucibles within a box furnace. The samples were intermittently extracted from the furnace and weighed throughout the tests to quantify the weight loss. Due to the absence of a defined shape suitable for dimensional measurements post-testing, only mass loss data was gathered and processed to evaluate the oxidation behavior of the alloys at the required conditions.

The M10Si, M10SiC2, M10SiC5, M10Si5 and M10SiC8 compositions were tested using box furnace at temperature 1300°C. The resulting weight loss curves are presented in Figure 6.24. Mass loss curve of M10Si at 1300°C

It was found that much of the weight loss observed for the temperature of 1300°C samples were the result of areas of damage where surface connected porosity resulted in internal oxidation. An example of this behavior was observed for whisker added samples tested at 1300°C that suffered catastrophic oxidation, Figure 6.25. Mass loss curves of M10SiC2, M10SiC5 and M10SiC8 at 1300°C. The failure mechanism observed, involving lamination cracks connected to interconnected porosity within the samples, significantly impacted densification during Spark Plasma Sintering (SPS). During oxidation, this internal porosity hindered the escape of MoO₃ vapor. This phenomenon is reasoned to increase the oxygen diffusivity within the glassy phase, thereby accelerating catastrophic oxidation of the material. This highlights the critical importance of achieving high density and minimizing porosity in MoSiB alloys to enhance oxidation resistance and overall performance at high temperatures.

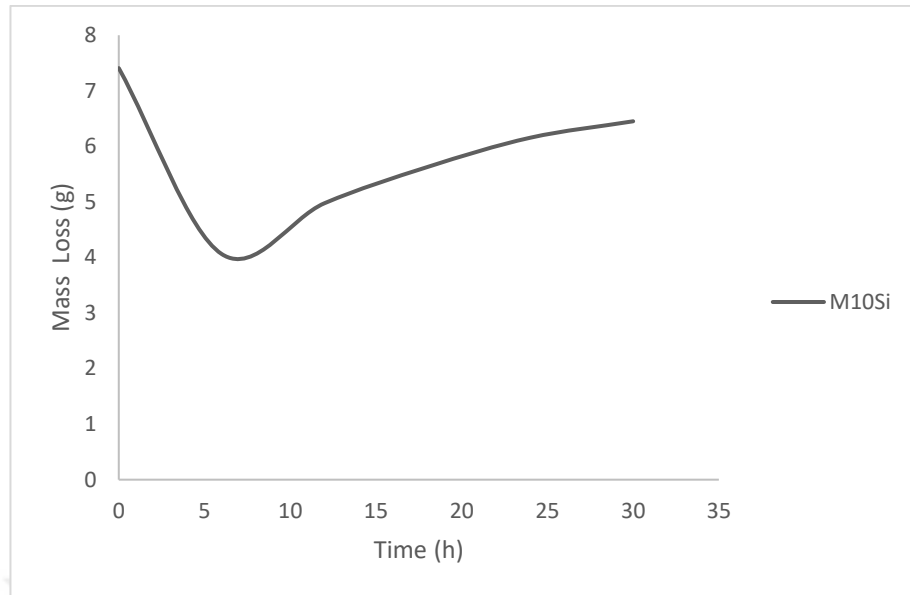


Figure 6.24. Mass loss curve of M10Si at 1300°C

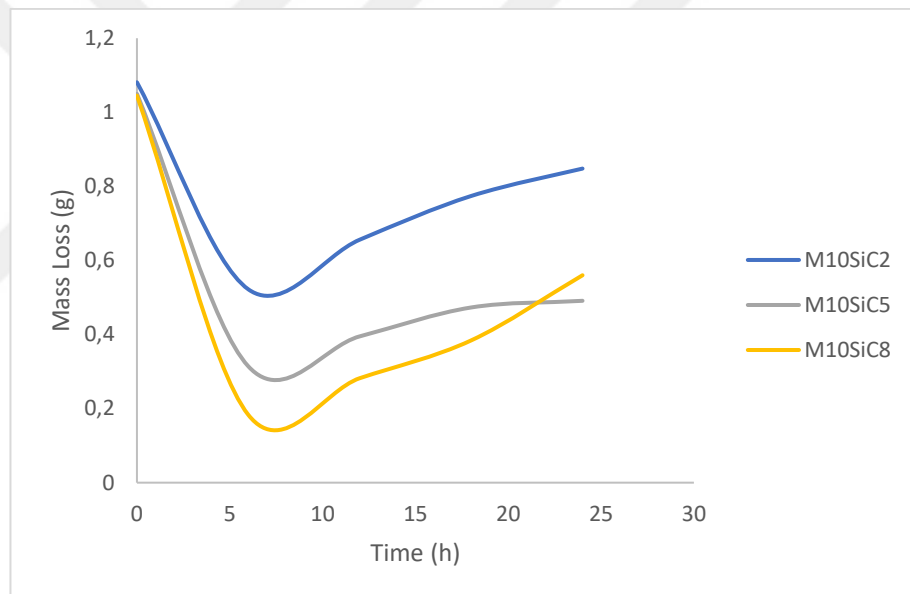


Figure 6.25. Mass loss curves of M10SiC2, M10SiC5 and M10SiC8 at 1300°C

Indeed, improving the microstructure of MoSiB alloys is essential for achieving a balance between oxidation resistance and mechanical qualities such as fracture and fatigue resistance. Elevated silicon and boron levels typically promote intermetallic production, hence improving oxidation resistance through the development of protective oxide layers. Conversely, attaining elevated volume fractions of the Moss phase enhances fracture and fatigue resistance through methods such as crack entrapment and toughening. Attaining an optimum microstructure necessitates meticulous regulation of alloy composition, processing techniques (such as powder metallurgy or SPS), and heat treatment parameters. This method enables customization of the material's properties to

satisfy particular application needs, whether in high-temperature settings such as gas turbines or in structural elements necessitating both strength and resistance to environmental deterioration. Ongoing enhancement in microstructural design will undoubtedly propel the progress and extensive application of MoSiB alloys throughout diverse industrial sectors.

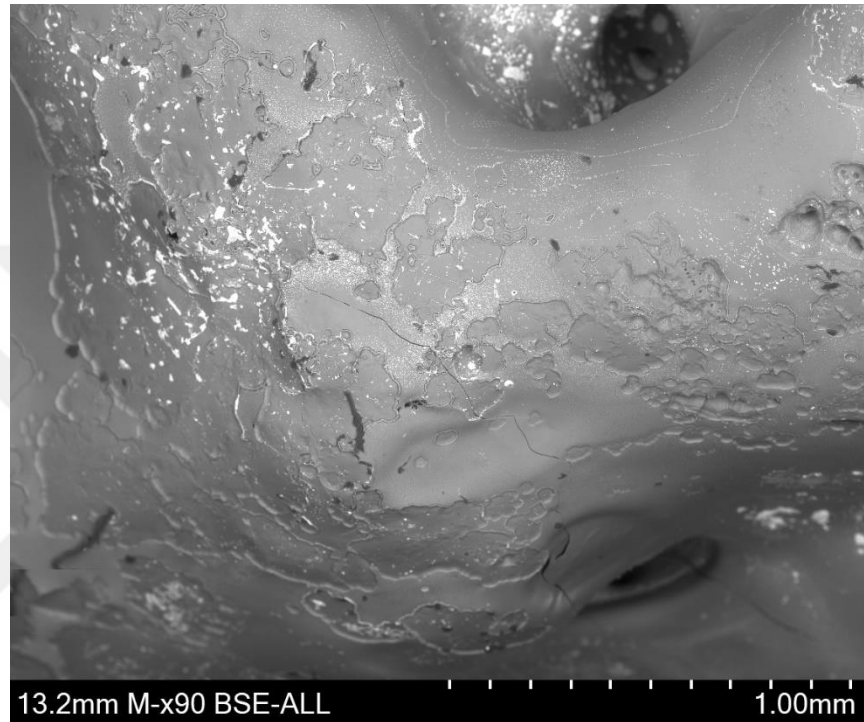


Figure 6.26. *Specimen oxidized surface modification of M10SiC2*

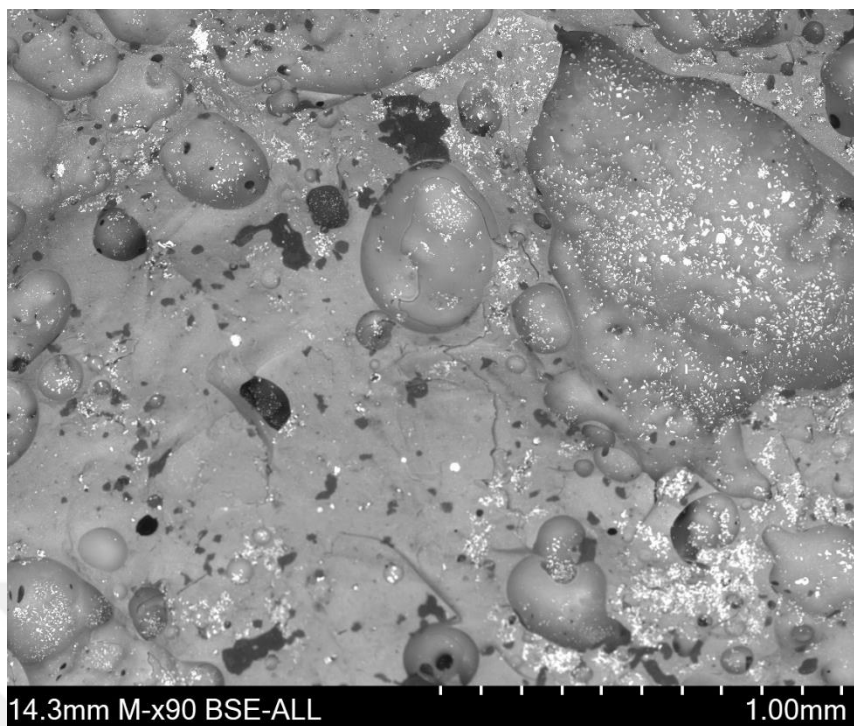


Figure 6.27. Specimen oxidized surface modification of M10SiC5

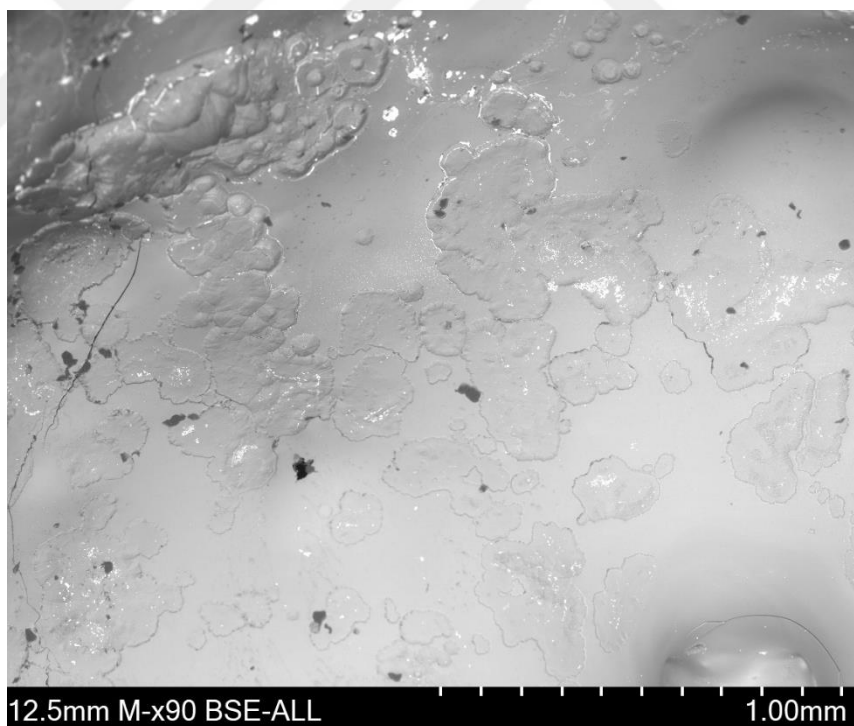


Figure 6.28. Specimen oxidized surface modification of M10SiC8

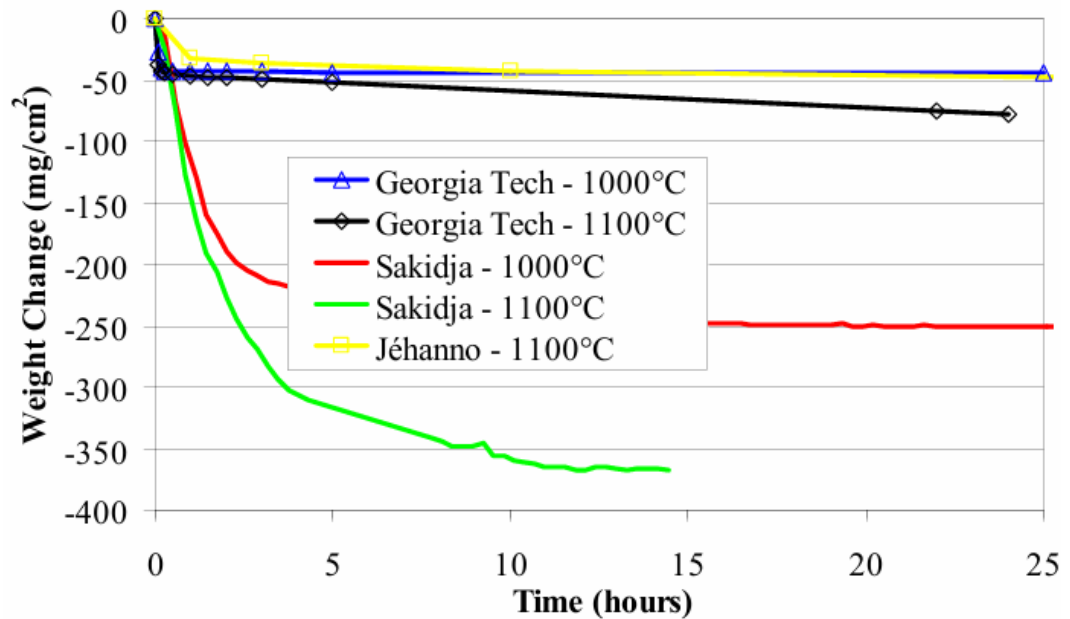


Figure 6.29. Oxidation of the Mo₃Si₁B wt.% alloy compared to similar test reported in the literature (R. Sakidja F. R., 2006). The error bars for the Georgia Tech data are within the data points

Investigating the intrinsic oxidation resistance of MoSiB alloys, particularly with the incorporation of SiC whiskers, is essential due to its relevance for applications involving thermal and environmental barrier coatings. These coatings are essential for improving the performance of components in elevated temperature conditions. Understanding the intrinsic oxidation resistance of the alloys is crucial, since any impairment to the coatings or oxide layers can undermine their efficacy.

This study examines the Mo₁₀Si₁₀B atomic percent alloy with varying weight percentages of SiC whisker additions at 1300°C. Through oxidation testing and averaging the weight losses from four samples, one may evaluate the impact of SiC whisker additions on the alloy's oxidation behavior. This information will yield critical insights into the performance of these alloys under oxidative circumstances and their applicability in high-temperature stability and oxidation resistance scenarios.

For the reported results in the literature, Figure 6.29. Alloys produced by reaction synthesis method have superior oxidation resistance compared to the alloy tested by Sakidja et al., which had long periods of transient weight loss. It can be saying that, the process type and addition rate of the alloy are of great importance in terms of oxidation testing.

6.5. Thermal Analysis

A combination of differential thermal analysis (DTA) and thermogravimetric analysis (TGA) is a robust approach for examining reactions, especially those involving oxide-based compounds, where weight loss can occur due to the evolution of oxygen scale.

Here is a breakdown of the experimental setup and procedures you described:

1. Instrumentation: The Netzsch Model 449 thermal analyzer was used for simultaneous TGA/DTA measurements.

2. Reference Standard: High purity alumina sample was the reference material for DTA measurements. It was pre-fired at 1450°C in air to eliminate any volatile compounds that could affect TGA results.

3. Measurement Conditions:

- Heating Rate: 10 K/min.

- Atmosphere: Flowing N₂/O₂. This atmosphere matches the firing conditions typically used for sintering processes.

These parameters guarantee that the measurements are performed in controlled surroundings that replicate the actual firing conditions employed for sintering. This facilitates precise assessment of temperature and mass alterations during reactions, especially those involving nitrogen release from nitride-based processes.

This configuration and approach are crucial for comprehending the thermal properties and reactivity of your materials. They offer significant insights on their processing and possible applications.

This study examines the Mo₁₀Si₁₀B atomic percent alloy with varying weight percentages of SiC whisker additions at 1300°C. Through oxidation testing and averaging the weight losses from four samples, one may evaluate the impact of SiC whisker additions on the alloy's oxidation behavior. This information will yield significant insights into the performance of these alloys under oxidative conditions and their applicability in high-temperature stability and oxidation resistance scenarios.

In this study discussing the thermal behavior and reactions of M₁₀Si, M₁₀SiC₂, M₁₀SiC₅, and M₁₀SiC₈ samples during heating. Here is a summary of the information you provided:

1. Initial Heating Behavior:

- At 697°C, there was a significant weight gain due to the formation of amorphous silica, likely induced by oxygen impurities.

- At 775°C, the sample started to lose weight, indicating a transformation of cristobalite silica.

- The corresponding DTA trace showed an exothermic peak due to the evolution of oxygen during these transformations.

- The M10Si sample decomposes at lower temperatures as it does not contain any SiC whisker addition.

2. Effect of Oxygen:

- Oxygen stabilized the silica reactants and influenced the temperature of the decomposition reaction, which occurred around 750-1300°C.

- The formation of silica also led to a volume increase, which could reduce the density of the samples.

3. Sintering Conditions:

- All alloys were sintered in an Ar/H₂ atmosphere to mitigate oxygen-related issues.

- However, it is noted that the powder mixtures were initially mixed in an open environment, not under inert conditions, which might have introduced oxygen impurities.

This information highlights the complex thermal and chemical interactions involved in the processing and behavior of MoSiB alloys, particularly regarding the influence of oxygen and its impact on silica formation and subsequent material properties.

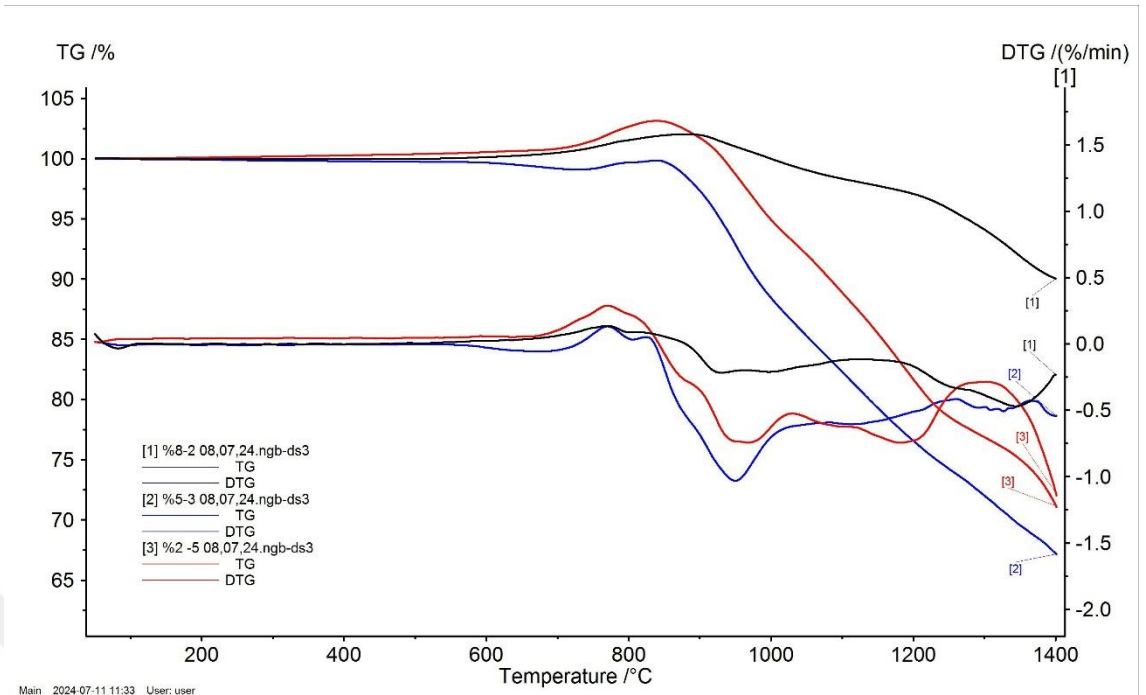


Figure 6.30. Combined TGA/DTA traces of all samples heated at 10 K/min in an atmosphere of N_2/O_2

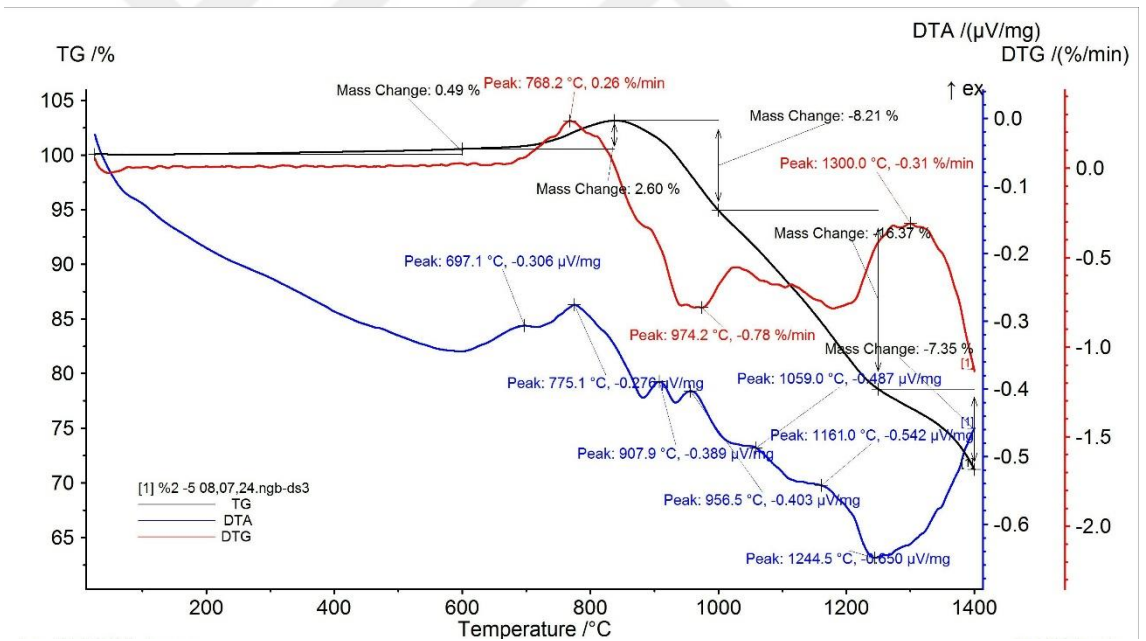


Figure 6.31. Combined TGA/DTA traces of M10SiC2 heated at 10 K/min in an atmosphere of N_2/O_2

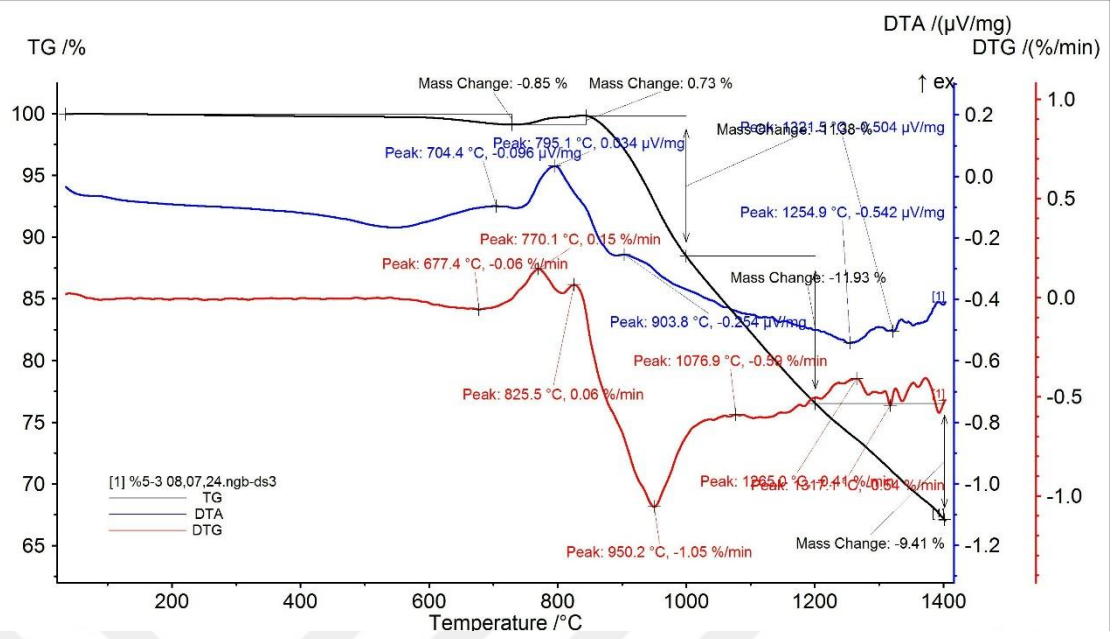


Figure 6.32. Combined TGA/DTA traces of M10SiC5 heated at 10 K/min in an atmosphere of N_2/O_2

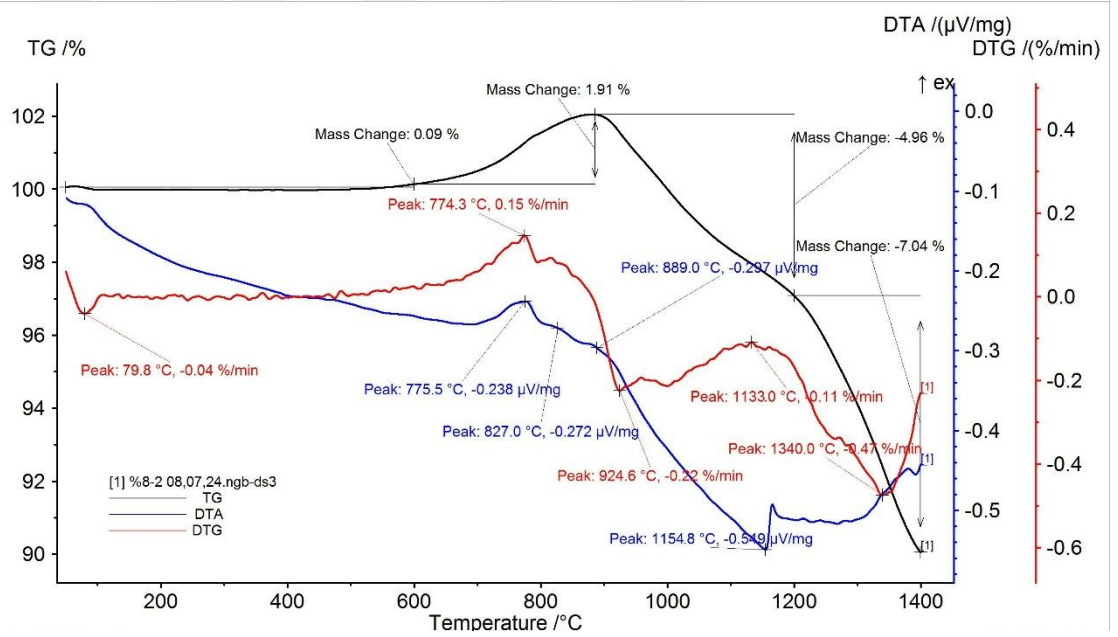


Figure 6.33. Combined TGA/DTA traces of M10SiC8 heated at 10 K/min in an atmosphere of N_2/O_2

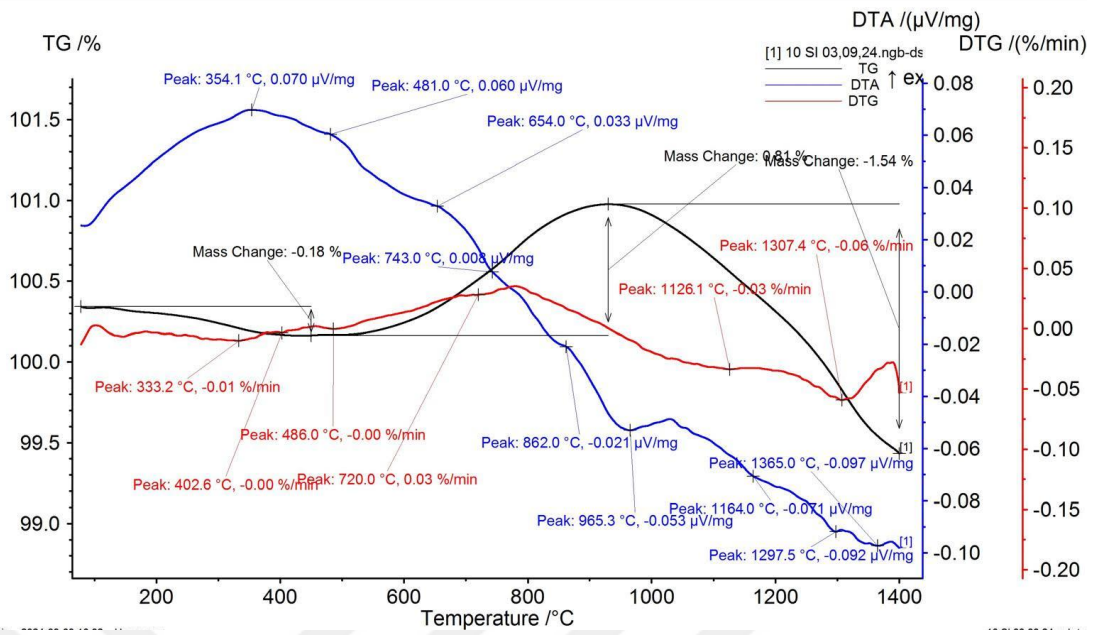


Figure 6.34. Combined TGA/DTA traces of M10Si heated at 10 K/min in an atmosphere of N₂/O₂

7. CONCLUSION AND FUTURE WORK

This study created a spark plasma sintering process that employs the reaction of molybdenum, silicon, boron, and SiC whisker powders to create a fine dispersion inside a MoSiB matrix. Covalent carbides have stability in oxidizing conditions up to 1000°C, hence enabling intermetallic processing. This technology utilizes conventional powder processing procedures, offering a simpler and more cost-effective means of producing MoSiB alloys than prior methods. Spark Plasma Sintering (SPS) is exceptionally proficient in generating dense materials, facilitating excellent densification of powders throughout the production phase. This approach simplifies the production process and improves the mechanical characteristics of the final MoSiB alloys. The alloys were sintered in a high-purity argon environment. Pressureless sintering at 1600°C did not attain densities over 95% of the theoretical value, while spark plasma pressing failed to achieve the complete theoretical density.

The formation of intermetallic phases (T1, T2, and A15) was investigated utilizing SEM and TGA techniques. The differentiation of intermetallic phases in backscatter-electron images impedes the comprehensive characterization of microstructures. The alloys' hardness was evaluated using a Vickers hardness tester with a 500 g load. The hardness values recorded were 16.92 GPa, 18.10 GPa, 13.64 GPa, 12.01 GPa, and 13.84 GPa, corresponding to the respective SiC whisker additions. These results demonstrate favorable hardness in comparison to those documented in the literature.

The oxidation characteristics of M10SiC2, M10SiC5, and M10SiC8 alloys were evaluated in air at 1300°C. After 6 hours, the weight loss attributed to surface layer development was 0.522 g for M10SiC2, 0.314 g for M10SiC5, and 0.183 g for M10SiC8. The weight loss noted after 24 hours was primarily ascribed to localized damage resulting from surface-connected porosity and interior oxidation. The results indicate that the incorporation of SiC whiskers is advantageous for minimizing mass loss.

The alloys hardness was tested using a Vickers hardness tester with a 500 g load, yielding values of 16.92 GPa, 18.10 GPa, 13.64 GPa, 12.01 GPa, and 13.84 GPa with SiC whisker additions, respectively. These values demonstrate promising hardness compared to literature values.

Oxidation tests of the M10SiC2, M10SiC5, and M10SiC8 alloys were conducted in air at 1300°C. After 6 hours, the weight loss due to surface layer formation was 0.522 g for M10SiC2, 0.314 g for M10SiC5, and 0.183 g for M10SiC8. Extended exposure for

24 hours increased weight loss, primarily from localized damage areas with surface-connected porosity leading to internal oxidation. These findings suggest that adding SiC whiskers is beneficial in reducing mass loss. The following the following recommendations are made for future research:

A fundamental issue recognized in powder metallurgy (PM) production is oxygen contamination, which is especially detrimental for silicon-containing alloys. High oxygen concentrations have typically been observed in sintered alloys. The oxygen concentration may be reduced by utilizing better purity powders and particularly by improving the process conditions for spark plasma sintering (SPS) to facilitate effective deoxidation. A substantial decrease in oxygen concentration may impede embrittlement and hence enhance fracture toughness. In this case, a clear strategy would be the comprehensive reduction of oxygen concentration within the alloy.

Subsequent endeavors should concentrate on consolidating the alloys at reduced temperatures to minimize grain sizes and lower the equilibrium concentration of silicon in the molybdenum-based matrix. This project should include ball milling to reduce agglomeration and improve the dispersion of raw materials. Furthermore, research is required to determine the duration for the precipitation of the A15 phase within the Moss matrix, taking into account annealing as a technique to diminish the silicon solid solution content. These methods can collectively improve the microstructural and mechanical characteristics of the MoSiB alloys.

REFERENCES

- Akinc, M. M. (1996). Isothermal oxidation behavior of mo-si-b intermetallics at 1450° c. *Journal of the American Ceramic Society*, 2763–2766.
- Baker, J. S. (1999). Refractory Metals Forum: Molybdenum Alloys and Emerging Applications. *Advanced Materials & Processes*, 61-66.
- Berczik, D. (1997). Patent No. 5,595,616.
- Berczik, D. (1997). Patent No. 5,693,156.
- C.A. Nunes, R. S. (2000). Liquidus Projection for the Mo-Rich Portion of the Mo-Si-B Ternary System. In *Intermetallics* (pp. 327-337).
- D. Sturm, M. H. (2007). The influence of silicon on the strength and fracture toughness of molybdenum. In *Materials Science and Engineering*.
- D.A. Helmick, G. M. (2005). The Development of Protective Borosilicate Layers on a Mo-3Si-1B (Weight Percent) Alloy,. *Metallurgical and Materials Transactions*, 3371-3383.
- D.M. Shah, D. B. (1992). Appraisal of Other Silicides as Structural Materials. In *Materials Science and Engineering* (pp. 45-47).
- Dimiduk, J. P. (2003). Mo-Si-B alloys: Developing a Revolutionary Turbine-Engine Material. *MRS Bulletin*, 639-645.
- Drawin, S. (2009). The European ULTMAT project: Properties of new Mo- and Nb-silicide based materials. *Mater. Res. Soc. Symp. Proc.*
- F. Chu, D. T. (1999). Processing and Properties of Mo₅Si₃ Single Crystals and Alloys. *MRS Symposium Proceedings*.
- H. Nowotny, E. D. (1957). Untersuchungen in den dreistoffsystemen: Molybdän-silizium-bor, wolfram-silizium-bor und in dem system. *Monatshefte für Chemie und verwandte Teile anderer Wissenschaften*, 180-192.
- Hansen, M. (1958). *Constitution of Binary Alloys*. New York: McGraw-Hill.
- J.E. Jackson, D. O.-J. (2007). Deposition and characterization of Al-Si metallic TBC precursor on Mo-Si-B turbine materials. *International Journal of Hydrogen Energy*.
- J.H. Perepezko, R. S. (2001). Phase Stability in Processing and Microstructure Control in High Temperature Mo-Si-B Alloys. *MRS Symposium Proceedings*.
- J.H. Perepezko, R. S. (2001). Phase Stability in Processing and Microstructure Control in High Temperature Mo-Si-B Alloys. *MRS Symposium Proceedings*.
- J.H. Schneibel, C. L. (1999). Microstructure and mechanical properties of Mo-Mo₃Si-Mo₅Si₂ silicides. In *Materials Science and Engineering* (pp. 78-83).
- J.H. Schneibel, J. K. (2003). Mo-Si-B Alloy Development . Pro, (p. Proceedings of the 17th Annual Conference on Fossil Energy Materials).

- J.H. Schneibel, M. K. (2001). Processing and mechanical properties of a molybdenum silicide with the composition mo–12si–8.5. *Intermetallics*, 25-31.
- J.J. Petrovic, A. V. (1999). Key Developments in High Temperature Structural Silicides. In *Materials Science and Engineering* .
- J.P.Wittenauer, J. W. (1993). The History and Development of Molybdenum Alloys for Structural Applications. *Evolution of Refractory Metals and Alloys*, 85-108.
- Koizumi, Y. (2004). Development of next-generation ni-base single crystal superalloys. *Proc. of the 10th International Symposium on Superalloys 2004*.
- Krüger, J. B. (2015). Impact of Phase Distribution on the Fracture Toughness of High Temperature Resistant Mo-Si-B Alloys. *Practical Metallography*, 295-313.
- Liao, K. S. (1988). The B-Mo (Boron-Molybdenum) System. *Bulletin of Alloy Phase Diagrams*, 457-466.
- M. Akinc, M. M. (1999). Boron-Doped Molybdenum Silicides for Structural Applications. In *Materials Science and Engineering*.
- M.K. Meyer, A. T. (1999). Oxide Scale Formation and Isothermal Oxidation Behavior of Mo-Si-B Intermetallics at 600-1000°C. *Intermetallics*, 153-162.
- Mitra, R. (2006). Mechanical behaviour and oxidation resistance of structural silicides. *International Materials Reviews*, 13-64.
- Ochiai, S. (2006). Improvement of the Oxidation-Proof Property and the Scale Structure of Mo₃Si Intermetallic Alloy through the Addition of Chromium and Aluminum Elements. *Intermetallics*, 1351-1357.
- P. Jain, A. A. (2006). High Temperature Compressive Flow Behavior of a Mo-Si-B Solid Solution Alloy. *Scripta Materialia*, 13-17.
- P. Jéhanno, M. H. (2004). Characterization of an Industrially Processed Mo-Based Silicide Alloy. *Intermetallics*, 1005-1009.
- P. Jéhanno, M. H. (2005). Assessment of a Powder Metallurgical Processing Route for Refractory Metal Silicide Alloys. *Metallurgical and Materials Transactions*, 515-523.
- R. Sakidja, F. R. (2006). Aluminum Pack Cementation of Mo–Si–B Alloys. *Scripta Materialia*, 903-906.
- R. Sakidja, J. P. (2008). Phase stability and structural defects in high-temperature mo–si–b alloys. *Acta Materialia*, 5223–5244.
- R.E.Honnell, J. P. (1990). SiC Reinforced- MoSi₂/WSi₂ Alloy Matrix Composites. *Ceram. Eng. Sci.Proc.*, 734-744.
- Ritchie, J. L. (2012). Mo-si-b alloys for ultrahigh-temperature structural applications. *Advanced Materials*, 3455-3480.
- Ritchie, J. L. (2012). Mo-si-b alloys for ultrahigh-temperature structural applications. *Advanced Materials*, 34450-3480.

- S.H. Ha, K. Y. (2012). Compositional regions of single phases at 1800° c in mo-rich mo–si–b ternary system. *Materials Science and Engineering*, 179-188.
- Schider, S. (1991). *Refractory Metals*.
- Schneibel, I. R. (2000). Stoichiometry and Mechanical Properties of Mo₃Si. *Intermetallics*, 885-889.
- T.A. Parthasarathy, M. M. (2002). Oxidation mechanisms in mo-reinforced mo₅sib₂ (t₂)–mo₃si alloys. *Acta Materialia*, 1857-1868.
- T.G. Nieh, J. W. (2001). Deformation of a Multiphase Mo-9.4Si 13.8B Alloy at Elevated Temperatures. *Intermetallics*, 73-79.



CURRICULUM VITAE

ORCID ID: 0009-0002-9487-7331

Name Surname : Buse KATIPOĞLU

Foreign Language : English

Education and Professional Background:

- **Master's degree** (Sep 2021 – Aug 2024)

Eskişehir Technical University

Institute Of Graduate Programs

Materials Science And Engineering

- **Bachelor's degree** (Sep 2012 – July 2017)

Ankara Yıldırım Beyazıt University

Faculty Of Engineering and Natural Sciences

Metallurgical and Materials Engineering Pr.

Professional Union/Association/Organization Memberships:

- **Quality Control Engineer**

Ankara- PANEL A.Ş.

Nov 2017 to July 2019

- **Lead Material and Process Development Engineer**

Eskişehir- Tusaş Engine Industries Inc.

Aug 2019- cont.

Skills:

- **COMPUTER AIDED 3D MODELING AND ANALYSIS (CATIA)**
- **ICAP 700 ICP-OES**
- **IHA-1-Sportive/Amateur Piloting**
- **Introduction to Reverse Engineering with Polyworks Modeler**